UNIVERSIDAD DE GRANADA

University of Granada
University of Roma Tor Vergata

Cycle XXIX

PhD program Physics and Space Science
PhD program in Astronomy, Astrophysics, and Space Science

Beyond standard model particle constraints from stellar evolution

Adrián Ayala Gómez

Advisors:
Dr. Inmaculada Domínguez Aguilera (UGR)
Dr. Oscar Straniero (INAF)
Coordinators:
Dr. Ángel V. Delgado Mora (UGR)
Dr. Pasquale Mazzotta (Tor Vergata)

Editor: Universidad de Granada. Tesis Doctorales
Autor: Adrián Ayala Gómez
ISBN: 978-84-9163-681-6
URI:http://hdl.handle.net/10481/48829

To my family, in particular to my mother and to Concha, who sparked the interest in Science.
To my teachers and mentors, specially those I never met... but read: Carl Sagan, Isaac Asimov and Richard Feynman.

Acknowledgements

This is not the easy part of the thesis to write. Looking back at the beginnings of the project, I'm conscious that I am in debt to many people who helped in one way or another. For some, it is with heartfelt gratitude for the pleasure of having met them during these years. I must apologize for not mentioning everybody in this Acknowledgement for it would take another long chapter. The following is not complete but it is significant:

I'm grateful to:

My advisors, for the opportunity of being involved in this exciting project, for their suggestions and for the topics I learned from them about stellar evolution and stellar models.

Maurizio Giannotti, Alessandro Mirizzi, Igor Irastorza and Javier Redondo for the many enlightening conversations about particle physics.

My colleague and friend Simon Verley, for his invaluable help and information about software, especially python, Linux OS, presentation skills and astrophysics.

Members of Fisica Teórica y del Cosmos, department of the University of Granada, for a number of good conversations, not always about science.

The staff of the Astronomical Observatory of Teramo, Italy, for sharing their knowledge with me, particularly their expertise on both observational and theoretical astrophysics.

My friends and colleagues of the Faculty of Science of Granada and the IAA (Andalusian Astrophysics Institute), in particular Rubén, Elena, Simon (again), Tomás, Pablo, Irene, Salva, Sara, Juan Carlos, Fabio, Antonio, Andy, Javi y Mari Angeles ... for the awesome moments during these years.

Diane Haun, for a bit of help with the English.

And, of course, last but far from least, my family.

I also acknowledge the financial support from the Spanish Ministry of Economy and Competitiveness Project MINECO-FEDER AYA2011-22460 and AYA2015-63588-P, and the FPI grant BES-2012-059666 (with the associated "estancias breves" EEBB-I-14-08490 and EEBB-I-15-09993). The International Postgraduate School of the University of Granada, financed a short stay with the grant "Fortalecimiento de las acciones de Cotutela".

Granada, July of 2017

Abstract

In this thesis we accomplished numerical simulations of "beyond standard model particle"(axion-like particles) emissions from low mass stars. We looked for observable effects of these emissions, the focus being on axion-like particles from the cores of horizontal branch stars.
We obtained a strong bound on the axion-photon coupling, $g_{a\gamma}$, from analysis of a sample of 39 Galactic Globular Clusters. As recognized long ago, the R parameter, i.e., the ratio of stars in the horizontal over the red giant branch of old stellar clusters, would be reduced by the axion production from photon conversions occurring in stellar cores. In this regard, we have compared the measured R with state-of-the-art stellar models obtained under different assumptions for $g_{a\gamma}$. We show that the estimated value of $g_{a\gamma}$, substantially depends on the adopted He mass fraction Y, an effect often neglected in previous investigations. Taking as a benchmark for our study the most recent determinations of the He abundance in extragalactic H_{II} regions with O/H in the same range as Galactic Globular Clusters, we obtain an upper bound $g_{a\gamma} < 0.66 \times 10^{-10}\,\mathrm{GeV}^{-1}$ at 95% confidence level. This result significantly improves the constraints from previous analyses and is currently the strongest limit on the axion-photon coupling from stellar evolution, in a wide axion mass range. A study of the uncertainties (considering both, theoretical and observational) is also performed.

Sommario

In questa tesi abbiamo ottenuto simulazioni numeriche dell'emissione di particelle non incluse nel "modello standard" in stelle di piccola massa. In particolare, dal confronto con un campione di 39 amassi globulari galattici, abbiamo ottenuto un limite superiore per la constante dell' accoppiamento assione-fotone. Era gia noto che il parametro R, ossia il rapporto fra il numero de stelle di ramo orizzontale ed il numero de stelle che si trovano nella parte più brillante del ramo delle giganti rosse diminuisce se si attiva la conversione di fotoni in assioni nell'interno di queste stelle. Abbiamo quindi confrontato il parametro R misurato negli ammassi globulari con quello ottenuto nelle simulazioni mumeriche per diverse ipotesi sull'accoppiamento fotone-assione. In questo modo troviamo che la costante di accoppiamento fotone-assione ($g_{a\gamma}$) dipende dalla frazione di massa di elio, un problema che era stato trascurato nei precedenti studi. Utilizzando le più recenti misure dell'abbondanza di elio nelle regioni H_{II} extragalattiche con O/H simile a quello degli amassi globulari, otteniamo il limite superiore $g_{a\gamma} < 0.66 \times 10^{-10}\, GeV^{-1}$ a un livello di confidenza de 95%. Questo risultato migliora i limiti delle analisi precedenti, essendo il più stringente derivato dell'evoluzione stellare in un intervalo di masse degli assioni ampio. Per concludere, viene presentato uno studio dettagliato delle incertezze teoretiche e osservative.

Resumen

Esta tesis trata acerca de simulaciones numéricas de la emisión, desde el interior de estrellas de baja masa, de axiones, partículas hipotéticas propuestas en ampliaciones del Modelo Estándar. Nos centramos en los posibles efectos, en observables de los cúmulos globulares, debidos a la producción de axiones y a su posterior emisión desde los interiores estelares.

A partir del análisis de una muestra de 39 cúmulos globulares galácticos, obtenemos un límite superior de la constante de acoplamiento entre el axión y el fotón, $g_{a\gamma}$. Investigaciones previas indican que el parámetro R, esto es, el cociente entre el número de estrellas en la rama horizontal y la rama de las gigantes rojas de los cúmulos globulares, disminuiría por la conversión de fotones en axiones, en el interior de esas estrellas. Con el fin de comprobar esta hipótesis, hemos comparado el parámetro R determinado observacionalmente con el predicho a partir de diversas simulaciones, en las que hemos introducido distintos valores de $g_{a\gamma}$. Demostramos que el valor estimado de $g_{a\gamma}$ depende sustancialmente de la abundancia inicial de helio de la estrella, Y, un efecto no considerado anteriormente. Tomando como referencia en nuestro estudio las determinaciones más recientes de la abundancia de helio, en regiones H_{II} extragalácticas con O/H en el mismo rango de los cúmulos globulares galácticos, obtenemos un límite superior $g_{a\gamma} < 0.66 \times 10^{-10}\ GeV^{-1}$ (95% de confianza). Este resultado mejora, de forma significativa, los análisis previos y es actualmente el límite más restrictivo de $g_{a\gamma}$, en un rango de masas del axión amplio y obtenido a partir de la evolucion estelar. La tesis concluye con un estudio de las incertidumbres observacionales y teóricas que afectan a nuestros resultados.

Contents

List of Figures

List of Tables

Chapter 1

Introduction

Contents

1.1 Beyond the "Standard Model"

Particle physics describes the Universe within an elegant frame, the Standard Model (SM), in which three generations of quarks and leptons and gauge bosons can account for all the observed particles. On the other hand, all the known forces among particles are mediated by bosons: gluons, in the case of strong nuclear force, and the three vectorial particles of electro-weak interaction (photon, $W^{\pm}$, and Z^0). This picture excludes for the moment gravity, even though a quantum field theory of gravitational force, mediated by bosons called gravitons, and unified with the other interactions into a common mathematical description is being sought. The phenomenology of particle physics is largely in agreement with the SM predictions.

Notwithstanding the great success of the standard model, unexplained phenomena suggest that further extensions of the theory are needed. These extensions would imply the existence of new fields and therefore new particles. Amongst motivations of these new particles, there are some problems in the strong interaction such as the Charge Parity (CP) conservation, which is not predicted by the SM. This mismatch of theory with observations can be solved by introducing a new scalar field, and the associated bosons, undergoing a dynamical symmetry breaking. These bosons are called axions, after Peccei & Quinn (1977a). On the other hand, the so-called "hierarchy problem", i.e. the too small mass of Higgs boson, compared to what would be expected because of the large quantum contributions, seems to point towards the introduction of a supersymmetry in the high energy limit of the SM. This hypothesis introduces new particles, the supersymmetric partners of standard bosons and fermions. Moreover, a great deal of astronomical observation supports the idea that the Universe is full of some kind of non-standard matter, the so called Dark Matter (DM), whose existence can be inferred from many observations in the field of extragalactic astrophysics (see, e.g. the reviews of Bertone & Silk (2010) and Drees & Gerbier (2012)).

Modern cosmology regards DM as a component of utmost importance in the Universe. Baryonic matter (i.e, common matter composed of quarks) is able to interact with electromagnetic radiation and indeed there is a large fraction of the mass of Galaxy Clusters, measured by indirect dynamical methods, which does not interact with photons, neither emitting nor absorbing them. This fraction is thought to be DM. The first evidence of the existence of it came from Zwicky (1933), who when measuring the "gravitational mass" of the Coma Cluster, discovered it exceeded luminous matter by an order of magnitude. Since this intriguing discovery, other probes, such as the rotation curves of spiral galaxies (Rubin et al. 1980; Persic et al. 1996b,a), the kinematics of galaxy clusters (Hayashi & White 2006), the study of gravitational lensing (Babul & Lee 1991) and the outcome of the

simulations of the large structure of the Universe, which requires the inclusion of DM (Springel et al. 2006), have added to previous hints. Today, we know about 27% of the mass-energy content of the Universe is DM (Perlmutter et al. 1998; Planck Collaboration et al. 2014).

Hence, several puzzling problems indicate the necessity of including SM in a more general frame, the Beyond Standard Model (BSM), where new particles are expected to exist. Beyond standard model theories can be related to SM high and low energy limits. The high energy limit, fixed after Large Hadron Collider (LHC) recent upgrades in the scale of TeV, introduces Weakly Interacting Massive Particles (WIMPs), proposed for many supersymmetric models and supported by the fact that a relic density of WIMPs may give an account of the hypothetical dark matter distribution (the so called WIMPs miracle). A low energy barrier deals with small mass bosons, in a range between μeV and keV, called Weakly Interacting Slim Particles (WISPs).

The astrophysical phenomenology requiring the action of some new physics is not limited to the existence of dark matter. The transparency of the Universe to high energy gamma-rays (de Angelis et al. 2007) and the observed luminosity of White Dwarfs (WDs) (Isern et al. 2008) seem to imply the existence of BSM physics. In addition, BSM would affect stellar structure and evolution. In this way astrophysical objects can be useful as particle physics laboratories while constraints on BSM can be derived from the comparison of stellar models and observations of stars.

1.2 WIMPs and WISPs

Partially motivated in the frame of Supersymmetry, WIMPs have both, a plausible mass and a "weak" (in the sense of weak interactions) coupling constant that explain the relic density of dark matter (Jungman et al. 1996). In addition, previous studies claimed WIMPs could be an additional energy source within stars near the halo region. If WIMPs are the main content of the halo it is expected they will be trapped inside stellar cores by gravitational interaction. The energy released by couples of particle-antiparticle (WIMP-anti WIMP) annihilation should be carried outside the star, producing, for example, a decrease in the rate of hydrogen burning. Constraints to WIMPs density in the halo are a result, excluding the densities which would imply a mismatch with the observed main sequence of some stellar populations (Lopes et al. 2011).

However, recent discoveries of the number and distribution of Milky Way

dwarf galaxy satellites, which could not be explained with WIMPs models, and the first results of the LHC experiments (Kowalska et al. 2015), where there is no evidence of supersymmetryc particles, have increased the interest in low mass WISPs as dark matter candidates. In addition, several ongoing experiments and proposals (Any Light Particle Search II (ALPS-II) and International Axion Observatory (IAXO), for example) are entirely devoted to the search for light, weakly interacting particles (Carosi et al. 2013).

This dissertation will deal with a kind of WISPs, the aforementioned axion. We use stellar evolution models to identify observables, which might impose constraints on axion properties and maybe shed light on the existence of this particle. The two main reasons for considering these particles in stellar astrophysics are the fact they can be produced by photon-photon or photon-charged lepton processes within the stellar plasma (Dine et al. 1981), due to their relatively low mass, and may account for the anomalous cooling found in several stellar evolution phases (Giannotti et al. 2016). Axions are of great interest at this moment and several new experiments are specifically designed to detect them. A study of axions within the stellar evolution approach benefits both fields, stellar physics and BSM theories.

Axions were initially introduced into the field of particle physics (Peccei & Quinn 1977b; Weinberg 1978) as the particles related to a new global symmetry, $U_{(1)}$. To explain the absence of a significant charge-parity violation for the strong interaction, which would imply a non-null electric dipole moment for the neutron, the so-called strong CP problem, the $U_{(1)}$ symmetry must be broken. More in detail, if Quantum Chromodynamics (QCD) lagrangian is considered, there is a term that violates CP symmetry:

$$\mathscr{L} = \theta \frac{\alpha_s}{8\pi} G_{\mu\nu} \tilde{G}^{\mu\nu} \quad , \tag{1.1}$$

where $G_{\mu\nu}$ and $\tilde{G}^{\mu\nu}$ are the symmetric and antisymmetric gluon field tensors and α_s is the strong coupling constant. The parameter θ is the so-called mixing angle, a quantum-mechanics phase. The QCD expected value of θ parameter can in principle be larger than that derived from experiments. The constraint on θ parameter relies on the experimental upper bound of the neutron electric dipole moment. For the electric dipole moment of the neutron, d_n, and θ the following relation (see the review of Graham et al. (2015)) holds:

$$d_n = -3.3 \times 10^{-16} \theta \quad . \tag{1.2}$$

Experimental research excludes d_n values larger than -2.9×10^{-26} $(e \cdot cm)$. Therefore, taking into account the equation 1.2, θ allowed values must satisfy the condition:

$$|\theta| < 9 \times 10^{-11}\,(e \cdot cm) \quad . \tag{1.3}$$

As QCD calculations indicate θ should be close to π, whereas the observed electric dipole moment of the neutron excludes θ values that rise higher than 10^{-10}. Therefore, some mechanism has to maintain the mixing angle under a certain value, otherwise CP violation and the observable neutron electron dipole would be larger. To solve this problem, Pecci and Quinn (Peccei & Quinn 1977b) proposed the existence of an additional global symmetry, called $U_{(1)}$ symmetry. The existence of this symmetry implies adding an additional term to the QCD lagrangian (a certain field, $a\,(t,x)$) cancelling the effect of the CP violating term:

$$\mathscr{L}' = \frac{1}{2}\partial^{\mu}a\partial_{\mu}a + C_a\frac{a}{f_a}\frac{g^2}{32\pi^2}G_a^{\mu\nu}\tilde{G_{\mu\nu}^{a}} \quad . \tag{1.4}$$

Where f_a is a free parameter, corresponding to a certain energy scale. Expanding the axion field around its vacuum expectation value and subtracting to CP violating term, an "effective mixing angle" appears:

$$\bar{\theta} = \theta - \frac{a}{f_a} \quad . \tag{1.5}$$

Thus, $\bar{\theta}$ has to vanish in order to minimize energy, and then $U_{(1)}$ symmetry is broken "dynamically". Oscillations of the effective angle around a minimum leaves the CP-symmetry practically conserved. This term introduces a new scalar field, whose associated particle is called the axion. Therefore, $\bar{\theta}$ is constrained to small values, oscillations around a minimum of the axion field. These oscillations are driven by a cosine term where the mass of the axion, m_a, which comes from QCD perturbative effects, is included, as is shown in Equation 1.6:

$$\bar{\theta} = \theta_0 cos(m_a t) \quad . \tag{1.6}$$

In Equation 1.6 the mass of the axion is introduced as the only free parameter. The axion mass, m_a, acquired due to QCD effects, is related to the scale of energy, f_a, which is proportional to vacuum expectation energy. Within this theoretical frame, the axion mass satisfies

$$m_a \approx 6eV\left(\frac{10^6 GeV}{f_a}\right) \quad . \tag{1.7}$$

Moreover, for QCD axions, m_a and f_a, satisfy the relationship

$$m_a = \frac{m_\pi f_\pi}{f_a} \quad , \tag{1.8}$$

where m_π and f_π are pion mass and pion decay constants. Equation 1.8 defines the so called axion-line (see, e.g. Kuster et al. (2008)).

Depending on the mass, axions can be considered DM candidates or not. Some axion models indicate that the existence of such particles could account for most or all of the cold dark matter in the Universe, more specifically models which consider axions with masses in the 10 μeV region (Kawasaki & Nakayama 2013; Di Valentino et al. 2014). For masses below 1 meV, coherent oscillations of axionic fields can make axions undergo a Bose-Einstein condensation (Sikivie & Yang 2009). The dynamical properties of this condensate are compatible with dark matter effects, because axions trapped in the condensate, can originate gravitational potentials which account for phenomena such as the relic density of dark matter and the satellite distribution around the Milky Way.

In general, Sikivie (2008), develops a relation between the mass of the axion and the dark matter density ($\Omega_{DM} = 0.23$). This relation is given by Equation 1.9

$$\Omega_a \approx \left(\frac{6\mu eV}{m_a}\right)^{7/6} \quad , \tag{1.9}$$

which indicates an approximate value for axion mass, $m_a \sim 20\ \mu eV$. There are also interesting theoretical frames for axions in the mass range $m_a =$ 60 meV, that would attain thermal equilibrium at the QCD phase transition or later (Turner 1987; Massó et al. 2002), contributing to the cosmic radiation density and, subsequently to the cosmic hot dark matter along with massive neutrinos (Archidiacono et al. 2013).

A general property of axions is the coupling with the electromagnetic field, given by the lagrangian term

$$\mathcal{L} = -\frac{g_{a\gamma}}{4} F\tilde{F} = g_{a\gamma}\mathbf{E}\cdot\mathbf{B} \quad , \tag{1.10}$$

where F and $\tilde{F}$ are the symmetric and antisymmetric tensors of the electromagnetic fields, whereas $g_{a\gamma}$, is the axion-photon coupling constant, defined by means of Equation 1.11

$$g_{a\gamma} = \frac{C_\gamma \alpha}{2\pi f_a} \quad , \tag{1.11}$$

α standing for the fine structure constant, whereas C_γ is a constant which depends on the models (Kim 1979; Dine et al. 1981). Due to the fact f_a is in the denominator, $g_{a\gamma}$ is proportional to the axion mass, and has dimensions of GeV^{-1}. In this dissertation g_{10} will stand for values of $g_{a\gamma}$, multiplied by

10^{10} GeV.

The coupling of axions with the electromagnetic field, produces axion decay in two photons, or in the reverse process, photon-axion conversion, as depicted in Figure 1.1. This process is pretty much analogous to the two-photon decay of another scalar particle, the pion, and is called the Primakoff process (see, e.g. Raffelt (1986)). The photon-axion conversion is a plausible way of axion production within stars, driven mainly by temperature and quenched by degenerate electrons. In addition, other axion production mechanisms exist, such as Compton photon-axion production or Bremsstrahlung (Dine et al. 1981). Depending on stellar conditions some mechanisms are favored or disfavored in comparison with others. The Primakoff mechanism is dominant in the stellar plasma conditions which are introduced in our simulations.

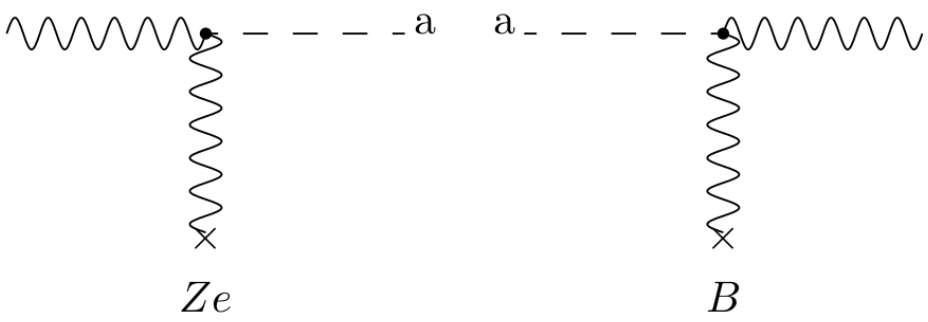

Figure 1.1: Primakoff process. Production of axions by means of photon conversion in the vicinity of an electromagnetic field (left). The inverse process, conversion of axions into photons in the presence of a magnetic field is also shown (right). The latter making possible the detection of axions in "light shinning through the wall" experiments.

In addition to the QCD formulation of axions, there are several theories which predict the existence of a new kind of light bosons called "axion-like particles" Axion-Like Particles (ALPs), which emerge in some theoretical frames (Essig et al. 2013; Jaeckel & Ringwald 2010). Even though they have a different motivation from QCD axions, the analogy between ALPs and "classical" axions is in the fact they both undergo Primakoff conversion into photons. In principle these particles do not hold any relation between the mass and axion-photon coupling constant, and in the parameter space these magnitudes are independent.

Ultra-light ALPs with a small coupling to photons would play an impor-

tant role in astrophysics. A particularly intriguing hint for these particles has been recently suggested by Very High-Energy gamma-ray experiments (de Angelis et al. 2007), even though this problem has also been analyzed using a more conventional physics (Essey & Kusenko 2010; Essey et al. 2010). Indeed, photon-axion conversions in large-scale cosmic magnetic fields would reduce the opacity of the universe to TeV photons, explaining the anomalous spectral hardening found in the Very High-Energy gamma-ray spectra (Horns & Meyer 2012).

1.3 Axion interactions with charged leptons and hadrons

It is necessary to distinguish the several interaction mechanisms between axions or axion-like particles and matter, in order to make an educated guess before design experiments or introduce axion production rates in stellar models. Most common theoretical frames of axion interactions are the models proposed by Kim, Shiftman, Vainshtein and Zakharov (KSVZ) (Kim 1979; Shifman et al. 1980) and Dine, Fischler, Srednick and Zhitnitskii (DFSZ) (Dine et al. 1981). The first model considers only axion-hadron interactions, whereas in the second model interactions between axions and charged leptons are also possible. In both models axion-photon coupling exist, and nowadays interactions with photons is a general property of axion and axion-like theoretical models.

The coupling of axions to electrons becomes important in some stellar interiors. Specifically, the most interesting types of axion-electron interaction that can occur in star interiors is a particular Compton scattering (Fukugita et al. 1982). Compton scattering consists of a photoaxion production, by means of an energy transfer between electrons and photons as shown in Equation 1.12,

$$\gamma + e \rightarrow e + a \quad . \tag{1.12}$$

In addition, models considering electron and axions interactions deal with Bremsstrahlung, a process which implies the emission of axions as the result of electron energy loss, in a process implying an electron-nucleus vertex like that of Equation 1.13,

$$e + [Z, A] \rightarrow [Z, A] + e + a \quad . \tag{1.13}$$

Another possibility is the production of an axion, besides a photon, by means of electron-positron pair annihilation. This process could happen instead of the usual neutrino antineutrino pair production resulting after

electron positron annihilation. However it is not expected to be as relevant as Compton or Bremsstrahlung, except for massive stars only, during the carbon burning phase. The process is described by Equation 1.14,

$$e^- + e^+ \rightarrow a + \gamma \quad . \tag{1.14}$$

From theoretical estimations, it is possible to derive expressions dependent on temperature and density of these processes, which predict if they can happen in a given stellar environment or not. Computed rates of Compton and Bremsstrahlung processes indicate that Compton increases as a T^6 function of temperature and is independent of density but decreases with electron degeneracy, whereas Bremsstrahlung requires high density, not being damped by degenerate electrons (Dine et al. 1981). Concerning the Primakoff effect, previous research (Raffelt & Dearborn 1987) indicates that the Primakoff rate is strongly damped by degeneracy and increases with temperature. Therefore, Bremsstrahlung is expected to take place in degenerate He and CO (carbon/oxygen) cores, like those of Red Giant Branch (RGB) and Asymptotic Giant Branch (AGB) stars respectively, whereas the Compton process could happen inside the He-burning non-degenerate cores of the so-called Horizontal Branch (HB) stars, or the He shell of the AGB phase. In the case of the Primakoff process, HB helium core is one of the best places where axions are expected to be emitted by means of this process.

1.4 Direct and indirect search for axions

The possibility of discovering WISPs in laboratory experiments or signals coming from space depends on the coupling between WISPs and standard model particles, especially photons. In particular the axion-photon coupling depends inversely on the energy scale, f_a, of the symmetry breaking responsible for this particle. A value large enough for f_a renders axions more weakly interacting with leptons, quarks and Higgs than neutrinos and in this case it is often referred to as an "invisible" axion.(Sikivie 1983). There are several ongoing experiments looking for axions specifically designed to take into account the mass range to be probed and therefore the coupling constant values. Among these experiments, are the CERN Axion Solar Telescope (CAST) or the future upgrade, IAXO (Irastorza et al. 2011). These helioscope experiments are searching axions emitted from the Sun, which are converted into x-ray photons when they pass through an intense magnetic field. On the other hand, there are experiments looking for axions in the mass range of μeV. These searches are of utmost interest for cosmological or DM axions. Among these experiments, ADMX (Duffy et al. 2006) exploits the conversion of cosmological axions into microwave photons in the presence of a magnetic field inside resonant cavities.

There are also pure laboratory experiments, such as Any Light Particle Search (ALPS) and its upgrade Any Light Particle Search II, ALPS-II, which try to directly produce axions and in general any light scalars, and then to detect them by exploiting the Light Shining through the Walls (LSW) effect. In this case, axions can go through physical barriers (walls) and, then, converted into photons when they enter a magnetic field region (inverse Primakoff process, see right panel of Figure 1.1). The photon excess with respect to the situation where a magnetic field is absent is proportional to the probability of conversion of axions into photons, given by the inverse Primakoff effect rate.

No definitive evidence of either kind of BSM particles, neither WISPs nor WIMPs, has been found so far. Most of the experiments have constrained parameter space regions, but have not confirmed the existence of new particles. The small interaction with common matter is usually invoked to explain the absence of events. Astrophysical indirect search of BSM particles is a complementary approach, looking for outer space signals, namely hypothetical gamma or x-ray radiation produced by the annihilation of dark matter particle-antiparticle pairs.

Figure 1.2 shows the excluded region of axion mass and axion-photon coupling constant. Limits obtain for coupling constant in ALPS and helioscope experiments for a fairly broad mass range $\left(10^{-12} - 10^{4}\right) eV$ are depicted as a black upper area. The KSVZ axion-line, corresponding to the linear relationship among m_a and f_a (or equivalently the inverse of $g_{a\gamma}$), which exists in case of QCD axions (see 1.8) is also shown. The different color areas show regions excluded by experiments and by arguments from stellar evolution. In particular, the figure shows the limits found by CAST experiment and the expected frontier which will reach IAXO.

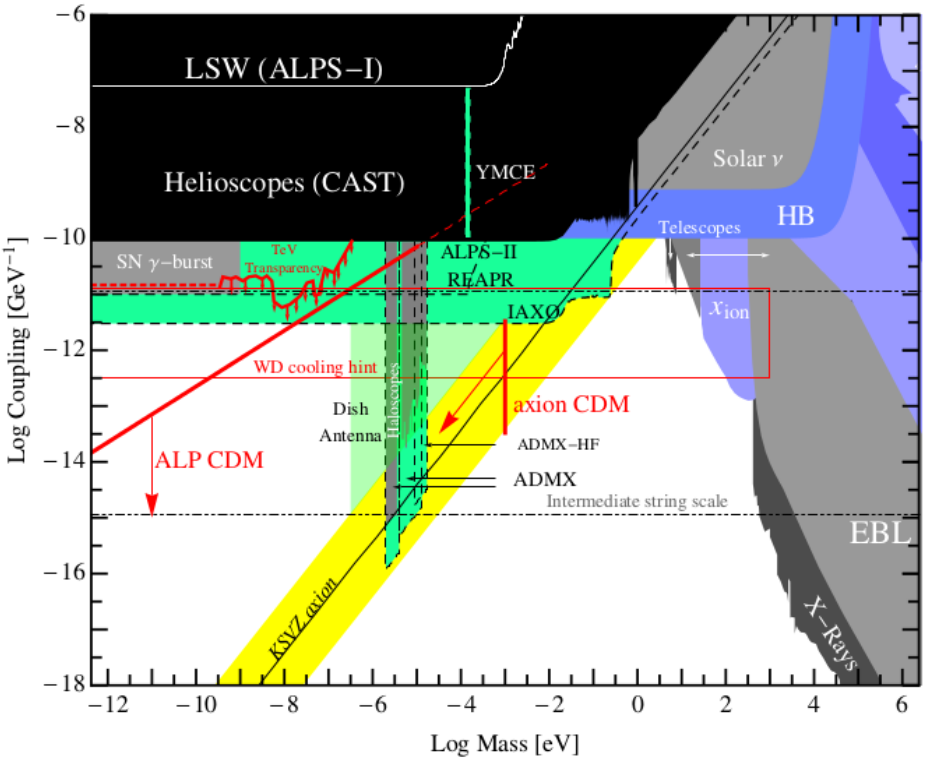

Figure 1.2: Parameter space of axions and ALPs: coupling constant vs mass. The Figure shows different regions excluded by experiments and astronomical evidence. Taken from Baker et al. (2013).

1.5 The stellar evolution approach

Gamow and Schoenberg were the first scientists who addressed the importance of weakly interacting particles, such as neutrinos inside stars, in particular the role of the neutrino in Supernovae processes (Gamow & Schoenberg 1941). As is well known, in normal stars like the Sun, neutrinos are produced by nuclear reactions or by thermal processes, among which are Compton, Bremsstrahlung, electron-positron annihilation or plasma oscillation processes (see Kippenhahn & Weigert (1990)). In this cases, due to the small cross section , neutrinos almost freely escape from stellar interiors, carrying away thermal energy.

Weakly interacting particle production inside stars is plausible if the mass of the particle is of the order of the thermal energy of the star core or lower, so that it can be produced by photon-lepton or photon-hadron or photon-photon processes (Kim 1987; Cheng 1988; Raffelt 1990) inside stars.

In case of axions, this occurrence implies that their mass should be smaller than a few keV in order to be produced in the core of hydrogen or helium-burning stars.

In recent years there has been a growing interest in the study of possible axion effects on stellar evolution. Specially on the existence of non-standard energy sinks in several types of stars can be explained invoking light particle emission from stellar cores (Giannotti et al. 2016). So, by producing stellar models that include axion production through the various thermal processes, and comparing the predicted theoretical outcomes with their observational counterparts, one may put constraints to the strength of the interaction between axions and SM particles like photons or electrons.

In more detail, the procedure to derive constraints on axions from stellar evolution, can be summarized in two steps:

1. Introduce in stellar models the production of axions, varying the free parameters, in our case the coupling to photons ;

2. Determine the axion parameters range which is consistent with observed stellar properties and therefore deriving constraints on axion models.

In the second step it is of paramount importance to take into account all the uncertainties affecting the predictions of the models. Moreover, the possibility of an additional effect, not considered in the models, which could be significant, may be a supplementary source of uncertainty in our analysis.

It should be recalled that our aim is to constrain axion models and in this way offer an aid to the experimental search of these particles. Indeed, even in case the inclusion of axions in stellar models could alleviate the tension between observations and stellar evolution, we cannot exclude the existence of additional uncertainties not considered in our analysis. On the other hand, our analysis can in any case provide reliable upper bounds to the axion parameters.

In this dissertation the determination of a new upper bound on axions and axion-like particles is achieved. The Primakoff conversion of two photons, a photon of stellar plasma and a virtual photon, into an axion is considered. The observable properties of Globular Clusters (GCs), populations of 10^4-10^8 stars, are used to impose constrains on axion models. This study deals with the evolution of a typical GC, low-mass star, with $Z = 0.001$ and circa $0.8\,M_{\odot}$. The observables used to derive bounds are, basically, the luminosity functions of GCs, which can be compared to stellar evolution

lifetimes. The number of stars at some evolutionary stages of a GC is influenced by processes that produce or consume energy in stellar interiors. These processes determine the times spent in different evolutionary phases. As we will explain in detail, an observable called R parameter (see Chapter 3) will be used in this thesis to constrain axion-photon coupling.

Chapter 2

Methods

Contents

2.1 Introduction

This chapter describes the code and physical inputs that we used to calculate stellar models. In particular, we present the adopted input physics: the nuclear network, electron screening, Equation of State (EOS), radiative and conductive opacities, mixing induced by convection, semiconvection and induced overshoot, and neutrinos production rate. In the final part of this chapter, we discuss the axion-photon interaction in stellar plasma, derive the rate of the energy carried away by axions, and estimate the stellar conditions which favour the Primakoff process (see section 1.2).

2.2 Theoretical stellar evolution

Astronomical observations give us information about the outermost layers of stars, the photosphere. In order to investigate the interior of stars it is possible to exploit asteroseismology and neutrino detection, but these techniques are mostly restricted to the Sun and to a few nearby stars. Consequently our knowledge of stellar interiors is mainly based on theoretical models performed by means of computer codes, whose predictions can be compared with astronomical observations. What we know about the internal structure of a star relies on our knowledge of the four fundamental interactions: a) nuclear forces, in particular those that control nuclear fusion, the process which supplies most of the energy of a star and accounts for the chemical evolution in the Universe; b) gravity, and c) electromagnetic interactions (Cox & Giuli 1968; Clayton 1983; Kippenhahn & Weigert 1990).

A star can be considered, most of its life, as a body in hydrostatic equilibrium between its own gravity and the thermal pressure of the plasma which constitutes most of its mass. Energy transport mechanisms are very important to understand the way a star evolves, in particular those driven by radiation, convection, and degenerate electron conduction. Modern stellar evolution theory benefits from developments in the field of nuclear reaction physics (Caughlan & Fowler 1988; Angulo et al. 1999; Adelberger et al. 2011), as well as from accurate models of convective mixing (Ledoux 1947; Böhm-Vitense 1958; Straniero et al. 2003).

The initial mass influences strongly stellar evolution. Since the relation between mass and luminosity of a star is not linear, the smaller the initial mass, the longer the stellar lifetime. In our work, we are interested in old stars, those belonging to GCs whose age is of the order of $13\,Gy$. We will concentrate our study in low mass stars ($M < 1\,M_{\odot}$).

2.3 Full Network Stellar Evolution Code (FUNS)

In this dissertation, we use the stellar evolution code FUNS, a lagrangian 1-D hydrostatic code, where mass, M, is set as an independent integration variable. A complete description of this code can be found in (Straniero et al. 2006; Cristallo et al. 2011, 2009). The code solves, by using the Heyney method, a full set of four first order, non-linear differential equations, describing: a) hydrostatic equilibrium, b) mass continuity, c) energy conservation, and d) energy transport. These equations are :

$$\frac{\partial P}{\partial M} = -\frac{GM}{4\pi R^4} \quad , \tag{2.1}$$

$$\frac{\partial R}{\partial M} = \frac{1}{4\pi R^2 \rho} \quad , \tag{2.2}$$

$$\frac{\partial L}{\partial M} = \epsilon_n + \epsilon_\nu + \epsilon_g \quad , \tag{2.3}$$

$$\frac{\partial T}{\partial M} = -\frac{GMT}{4\pi R^2 P}\nabla \quad . \tag{2.4}$$

As usual P, R, L, T and ρ represent pressure, radius, luminosity, temperature and mass density, respectively. In addition, ϵ_n, ϵ_ν, and ϵ_g in equation 2.3 stand for the energy production/loss rates per unit mass and time as due to nuclear reactions, thermal neutrinos processes and gravitational contraction or expansion. The symbol ∇ in Eq. 2.4 is the temperature gradient, $\nabla = \left(\frac{dlnT}{dlnP}\right)$. In case of energy transported exclusively by radiation, this should be

$$\nabla_{rad} = \frac{3}{16\pi acG}\frac{\kappa LP}{MT^4} \quad , \tag{2.5}$$

where κ stands for opacity. In case of adiabatic convection ∇ equals

$$\nabla_{ad} = \frac{\gamma - 1}{\gamma \chi_T} \quad , \tag{2.6}$$

where γ is defined as the ratio of specific heats at constant pressure and volume, c_P/c_V, and χ_T is the logarithmic derivative of P vs T, at constant ρ and chemical composition for each specie, Y_i :

$$\chi_T = \left(\frac{dlnP}{dlnT}\right)_{\rho, Y_i} \quad . \tag{2.7}$$

The FUNS code uses the Henyey method (Henyey et al. 1965) to solve the system of equations 2.1-2.3.

Stars evolve because they lose energy and because nuclear reactions modify the internal composition. Energy lost by photons, neutrinos and eventually additional cooling mechanism due to new particles, is continuously sustained by gravitational energy release and nuclear reactions, as shown in Eq. 2.3.

2.3.1 The equation of state

In order to calculate ρ, γ and χ_T, an appropriate EOS is needed. In the FUNS code two separate regions are distinguished :

- High temperature (Log $T > 6$), where matter can be assumed completely ionized. A set of tables of thermodynamic quantities (Straniero 1988), taking into account electronic degeneracy and relativistic effects, electron-positron pair production and Coulomb interactions among ions and electrons, are interpolated.

- Low T region (Log $T < 6$), where partial ionization may take place. The thermodynamic properties of partially ionized matter are calculated by means of the Saha equation. Partial ionization of the main chemical species (in particular hydrogen and helium) is taken into account, as well as the formation of H_2 and H_2^+ molecules. At high densities, full pressure ionization due to the depression of continuous is also considered.

2.3.2 Opacities

Opacity represents the probability of photons to interact with stellar plasma. The mean free path, l_{ph}, of a photon at an average point inside a star is defined as

$$l_{ph} = \frac{1}{\kappa_{rad} \cdot \rho} \quad , \tag{2.8}$$

where κ_{rad} is a mean absorption coefficient, i.e. a radiative cross section per unit mass averaged over frequency. Note that, in general, the radiative cross section depends on the photon frequency. Then, it is calculated using the Rosseland mean

$$\frac{1}{\kappa_{rad}} = \frac{\pi}{acT^3} \int_0^\infty \frac{1}{\kappa_\nu} \frac{\partial B}{\partial T} d\nu \quad . \tag{2.9}$$

Where B denotes Planck function for black body radiation, and κ_ν is the frequency dependent absorption coefficient.

In addition to the radiative transfer, the contribution of conduction due to electrons must also be taken into account. It can be done by defining a "conductive opacity", κ_{cd} (see, for instance, Kippenhahn & Weigert (1990)

and Cox & Giuli (1968)). If the flux carried by thermal conduction, F_{cond}, is considered, it holds

$$F_{cond} = -\nu_c \nabla T \quad , \tag{2.10}$$

where ν_c is the so-called coefficient of thermal conduction. In analogy with radiative transfer (see, Cox & Giuli (1968)), F_{cond} also satisfies

$$F_{cond} = -\frac{c}{\kappa_{cd} \cdot \rho} \nabla (\frac{1}{3} a T^4) \quad , \tag{2.11}$$

where the conductive capacity, κ_{cd} appears in the denominator. Comparing Eqs. 2.10 and 2.11, κ_{cd} can be written as

$$\kappa_{cd} = \frac{4acT^3}{3\nu_c \rho} \quad . \tag{2.12}$$

The simultaneous action of radiative and conductive opacities, implies that an overall opacity can be written as it is shown in Eq. 2.13:

$$\frac{1}{\kappa} = \frac{1}{\kappa_{rad}} + \frac{1}{\kappa_{cd}} \quad . \tag{2.13}$$

For the Rosseland radiative opacity at $T < 10^4$ we use the tables given by Alexander & Ferguson (1994), whereas in the case of $T > 10^4$ the tables computed by Iglesias & Rogers (1996) are considered. For conductive opacity, we adopt the values obtained by Potekhin et al. (1999).

2.3.3 The nuclear network

Usually about 700 isotopes are included in the nuclear network of the FUNS code. However, to perform the calculations of this dissertation, a reduced network, consisting of only 30 isotopes was adopted. These isotopes are listed in Table 2.1. Initial isotope abundances are taken from Lodders (2003), properly scaled with the assumed solar metallicity. For the initial He abundance we usually adopt the primordial value as determined from extragalactic low metallicity molecular clouds (Izotov et al. (2013); Aver et al. (2013), see the discussion in Chapter 4).

The H-burning and He-burning nuclear reactions considered are shown in Tables 2.2 and 2.3. In hydrogen burning zones the reaction rates listed in Adelberger et al. (2011) are adopted for both the $p-p$ chain and CNO cycle. In particular for the $^{14}N(p,\gamma)^{15}O$ reaction rate the low energy measurements obtained by the LUNA collaboration are exploited (Imbriani et al. 2005). Concerning the helium burning, the reaction rates of the two main processes, 3α and $^{12}C(\alpha,\gamma)^{16}O$ reactions, are taken from Caughlan & Fowler (1988) and Schürmann et al. (2012).

Nuclear reaction rates are corrected for the effect of electron screening. The electron screenings are taken from Graboske et al. (1973) and Dewitt et al. (1973) respectively for the weak-intermediate and intermediate-strong regimes, and from Itoh et al. (1977) and Itoh et al. (1979) for the strong regime.

2.3.4 Neutrinos

Energy carried away by neutrinos are taken into account in two different ways:

- The energy carried away by neutrinos or antineutrinos produced by β-decay or other nuclear processes are directly subtracted to the Q value of the specific reaction.
- The energy sink due to thermal neutrinos, namely those produced by Compton, Bremsstrahlung, pair annihilation, and plasma oscillation, is considered in the equation of energy conservation 2.3. The corresponding production rates are calculated according to Esposito et al. (2003)

2.3.5 Convection

Convection, the internal macroscopic mass transfer inside stars, as a result of stellar layers instabilities, takes place when the so-called "Schwarzschild's criterion" holds,

$$\nabla_{ad} \leq \nabla_{rad} \quad . \tag{2.14}$$

In this case the stellar regions where 2.14 is satisfied, become unstable under convection and convective heat transport happens. The regions which hold 2.14 are called convective regions, and their limits, "convective borders". These borders are found where radiative gradient equals exactly the adiabatic one, $\nabla_{rad} = \nabla_{ad}$. Since the radiative gradient depends on the radiative flux and the opacity (see Equation 2.5) the convective border changes with time according to the variation of these quantities. For instance during the core helium burning phase (HB stars) since helium is converted into carbon and oxygen, the opacity increases in the core and, in turn, the radiative gradient also increases. As a consequence, the external border of the convective core moves outside.

The effective thermal gradient (i.e. ∇ in Equation 2.4) is calculated in the frame of the mixing-length theory, following the prescriptions described in Cox & Giuli (1968). In this way, the effective gradient is always intermediate between the adiabatic and radiative gradient:

Table 2.1: List of the isotopes of the reduced network. The table shows isotopes, mass number, atomic number, and binding energies (erg).

Isotope	A	Z	$E_{binding}$ (erg)
^{1}H	1	1	0.0
^{3}He	3	2	0.0000124317654
^{4}He	4	2	0.000045364245
^{12}C	12	6	0.000147659677
^{14}N	14	7	0.000167718728
^{16}O	16	8	0.000204404096
^{2}H	2	1	0.00000358928562
^{7}Li	7	3	0.000630197686
^{7}Be	7	4	0.0000603873448
^{13}C	13	6	0.000155624706
^{15}N	15	7	0.000185040132
^{17}O	17	8	0.000211096343
^{18}O	18	8	0.000223984657
^{19}F	19	9	0.000236784362
^{20}Ne	20	10	0.000257284598
^{21}Ne	21	10	0.000268135911
^{22}Ne	22	10	0.000284708376
^{23}Na	23	11	0.000298776693
^{24}Mg	24	12	0.000317445451
^{25}Mg	25	12	0.000329201735
^{26}Mg	26	12	0.000346929014
^{27}Al	27	13	0.000360166705
^{28}Si	28	14	0.000378662287
^{29}Si	29	14	0.000392232567
^{30}Si	30	14	0.000409190515
^{52}Cr	52	24	0.000730316879
^{56}Fe	56	26	0.000787769744
^{57}Fe	57	26	0.000800028687
^{58}Ni	58	28	0.000810532912
^{60}Ni	60	28	0.000843127473

Table 2.2: Nuclear reactions in H-burning zones

Reaction	Reference
$^{3}He(^{3}He\,\alpha)2P$	Adelberger et al. (2011)
$^{3}He(\alpha,\gamma)^{7}Be$	Adelberger et al. (2011)
$^{1}H(^{1}H,\gamma)^{2}H$	Adelberger et al. (2011)
$^{2}H(^{1}H,\gamma)^{3}He$	Adelberger et al. (2011)
$^{7}Li(^{1}H,\alpha)^{4}He$	Adelberger et al. (2011)
$^{7}Be(^{1}H,\gamma)^{8}B$	Adelberger et al. (2011)
$^{7}Be(\nu,\gamma)^{7}Li$	Adelberger et al. (2011)
$^{12}C(^{1}H,\gamma)^{13}C$	Adelberger et al. (2011)
$^{13}C(^{1}H,\gamma)^{14}N$	Adelberger et al. (2011)
$^{14}N(^{1}H,\gamma)^{15}O$	Imbriani et al. (2005)
$^{15}N(^{1}H,\gamma)^{16}O$	Adelberger et al. (2011)
$^{15}N(^{1}H,\alpha)^{12}C$	Adelberger et al. (2011)
$^{16}O(^{1}H,\gamma)^{17}F$	Adelberger et al. (2011)
$^{17}O(^{1}H,\alpha)14^{N}$	Adelberger et al. (2011)
$^{17}O(^{1}H,\gamma)^{18}F$	Adelberger et al. (2011)
$^{18}O(^{1}H,\alpha)^{15}N$	Adelberger et al. (2011)
$^{19}F(^{1}H,\gamma)^{20}Ne$	Adelberger et al. (2011)
$^{19}F(^{1}H,\alpha)^{16}O$	Adelberger et al. (2011)

Table 2.3: Nuclear reactions in He-burning zones

Reaction	Reference
3α	Caughlan & Fowler (1988)
$^{12}C(\alpha,\gamma)^{16}O$	Schürmann et al. (2012)
$^{14}N(\alpha,\gamma)^{18}F$	Görres et al. (2000)
$^{16}O(\alpha,\gamma)^{20}Ne$	Costantini et al. (2010)
$^{18}O(\alpha,\gamma)^{22}Ne$	Kaeppeler et al. (1994)

$$\nabla_{ad} \leq \nabla \leq \nabla_{rad} \quad , \tag{2.15}$$

In the case of a convective core, because of the large heat capacity of matter, the superadiabaticity is generally small. On the contrary, in convective stellar atmospheres, the effective temperature gradient may approach the radiative one.

2.3.6 Mixing

In FUNS code a time-dependent mixing is considered in convective regions. We follow the approach introduced by Sparks & Endal (1980) and described by Langanke et al. (2006). With this approach the mass fraction, X_j, of a certain isotope at the mesh point, j, inside a convective region of mass M_{conv} is given by

$$X_j = X_j^0 + \frac{1}{M_{\rm conv}} \sum_k (X_j^0 - X_k^0) f_{j,k} \Delta M_k \quad , \tag{2.16}$$

where the summation is expected over the whole convective region and the superscript 0 refers to unmixed abundances. ΔM_k stands for the mass of the mesh point k. The damping factor, f is defined as

$$f_{i,k} = \frac{\Delta t}{\tau_{j,k}} \quad , \tag{2.17}$$

if $\Delta t < \tau_{j,k}$, or

$$f_{j,k} = 1 \quad , \tag{2.18}$$

if $\Delta t \geq \tau_{j,k}$. We define Δt as time step and $\tau_{j,k}$ is the mixing turnover time between points j and k, given by Eq 2.19

$$\tau_{j,k} = \sum_{r(j)}^{r(k)} \frac{dr}{v(r)} = \sum_{i=j,k} \frac{\Delta r_i}{v_i} \quad . \tag{2.19}$$

In Eq. 2.19, (v_i) stands for "mixing velocity", computed by means of the mixing-length theory, according to Cox & Giuli (1968), whereas Δr_i is the length of the mesh point i. The algorithm we have described, allows the calculation of the partial missing when the time step is reduced below the mixing timescale.

2.3.7 Induced overshoot and semiconvection

Along HB phase a discontinuity of opacity forms at the external border of the convective core as a consequence of the conversion of He into C (and O). Because of the higher opacities of carbon and oxygen, the radiative gradient increases. This phenomenon has two consequences. First, the border of the

fully convective core moves outwards (this is the so-called "induced overshoot"), and second, a semiconvective layer forms (see left panel in Figure 2.1).

On the other hand, the effect of mechanical overshoot, the inertia of the material accelerated by buoyancy forces, taking place at the boundary of the convective region should be considered, although the value of the overshoot parameter is unknown. As demonstrated by Straniero et al. (2003), in the core He-burning phase, a moderate mechanical overshoot mimics the effect of the induced overshoot. On the contrary, a large mechanical overshoot, namely of $1\,H_p$ or larger, where H_p indicates pressure scale height, would cancel out the semiconvective zone (see right panel of Figure 2.1).

In the FUNS code induced overshoot and semiconvection are included. The basic steps of the algorithm are:

- Starting from the formal convective border, a small overshoot is applied;
- Convective instability is checked (See Equation 2.15). If Equation 2.15 is fulfilled, a further overshoot is applied. If not, the overshoot is reduced at the external border or inside the well mixed region (convective border plus semiconvective region);
- In case of semiconvection, a detached convective shell forms and moves outward till $\nabla_{ad} = \nabla_{rad}$.

Therefore, the algorithm determines the borders of the convective core as well as the extension of the semiconvective layers.

Differences in the internal profiles of helium for semiconvective and mechanical overshoot models with $1\,H_p$ are shown in Figure 2.1. For central helium mass fractions smaller than 0.66, semiconvection induces a slope in the profile, corresponding to an outermost partially mixed region, instead of the abrupt variation of mechanical overshoot models.

Induced overshoot, semiconvection and mechanical overshoot influence HB lifetime, t_{HB}, because of the increase of the convective core and the injection of fresh He that they produce.

2.3.8 Mass loss

Mass loss from outer layers in stars has to be taken into account. In case of RGB and HB phases, FUNS code compute mass loss rate by means of

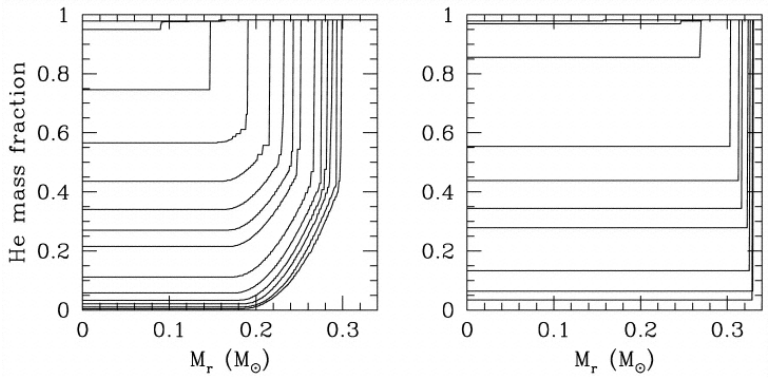

Figure 2.1: He mass fraction profiles vs $M/M_{\odot}$. Comparison of semiconvective (left) and mechanical overshoot (right) models. Taken from Straniero et al. (2003).

Reimers' formula:

$$\dot{M} = 1.34 \times 10^{-5} \eta \frac{L^{3/2}}{M T_{\rm eff}^2} \quad , \tag{2.20}$$

where $\dot{M}$ has dimensions of solar mass per year. The Reimers parameter, η is varied in order to describe the color spread of HB stars. The range of η explored in our calculation is between 0.1 and 0.4.

2.4 Primakoff two photons interaction

In this section a detailed calculation of the rate of Primakoff process is performed, from first principles. We work in the Lorentz-Heaviside units system . In this system, $\alpha = e^2/4\pi$ and the Poisson's equation is $\nabla^2\psi = -\rho$. We follow the notation and conventions from Raffelt & Dearborn (1987).

The axion-photon Lagrangian is:

$$\mathscr{L} = -\frac{g}{4} F\tilde{F} = gE \cdot B \quad . \tag{2.21}$$

The electromagnetic field has a radial and an external component. So, $\mathbf{E} = E_{ext} + \mathbf{E}_{\rm rad}$ and $\mathbf{B} = \mathbf{B}_{\rm ext} + \mathbf{B}_{\rm rad}$.

Of all the terms, we keep only

$$\mathscr{L} = g\mathbf{E}_{ext} \cdot \mathbf{B}_{\rm rad} = g\mathbf{E}_{ext} \cdot \nabla \times \mathbf{A} \,, \tag{2.22}$$

We consider the external field to be static, so that q has no temporal component. The space component of q, the 3-dimensional momentum transferred is denoted by $\mathbf{q}$.

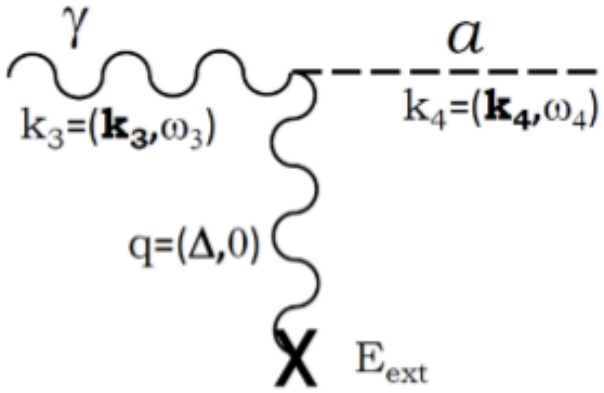

Figure 2.2: Detailed Feynman diagram of Primakoff process, showing the momentum transfer (q) between an incoming photon (k_3), and a virtual photon. An outgoing axion of four-momentum k_4 is produced.

2.4.1 Scattering Amplitude

Using the Feynman rules, the amplitude $\mathcal{M}$ equals

$$\mathcal{M} = g_{a\gamma}\mathbf{E}_{\text{ext}}(q)\cdot(\mathbf{k}_3\times\varepsilon) = g_{a\gamma}\,\varepsilon\cdot(\mathbf{E}_{\text{ext}}(q)\times\mathbf{k}_3)\ , \tag{2.23}$$

where ε stands for the photon polarization.

The Fourier transform of the external electric field can be found (in CGS units) from the scalar potential ψ as $\mathbf{E} = -\nabla\psi$ with $\nabla^2\psi = -\rho$, which implies $\psi = \rho/q^2$, and then

$$\mathbf{E} = i\mathbf{q}\,\frac{\rho}{q^2}\,. \tag{2.24}$$

It is useful to define the form factor as a normalized Fourier transform of the charge density

$$F(\mathbf{q}) = \frac{\rho(\mathbf{q})}{Ze} = \frac{1}{Ze}\int \rho(x)e^{i\mathbf{q}\cdot\mathbf{x}}d\mathbf{x}\,, \tag{2.25}$$

which equals 1 for a point charge (that is, for $\rho = Ze\,\delta(\mathbf{x})$). Thus, as $\rho = ZeF(\mathbf{q})$, it holds $\mathbf{E}_{\text{ext}} = iZeF(\mathbf{q})\mathbf{q}/q^2$. From the definition of $\mathcal{M}$, Equation 2.23, we find

$$\mathcal{M} = iZeg_{a\gamma}\frac{F(\mathbf{q})}{q^2}\,\varepsilon\cdot(\mathbf{q}\times\mathbf{k}_3) \quad . \tag{2.26}$$

Since $\mathbf{q} = \mathbf{k}_4 - \mathbf{k}_3$, it follows $\mathbf{q}\times\mathbf{k}_3 = \mathbf{k}_4\times\mathbf{k}_3$. Also, we average over the photon polarizations and obtain,

$$|\mathcal{M}|^2 = \frac{1}{2}\,(Ze\,g_{a\gamma})^2\,\frac{|F(\mathbf{q})|^2}{q^4}\,|\mathbf{k}_4\times\mathbf{k}_3|^2\ . \tag{2.27}$$

2.4.2 Cross section

The cross section is defined as the probability of interaction times density of final states divided by the incident flux. In this case, the incident flux is $2\omega_3$ and the density of final states is $\frac{d^3\mathbf{k}_4}{(2\pi)^3\,2\omega_4}$. Therefore,

$$d\sigma = \frac{1}{2\omega_3}\,\frac{d^3\mathbf{k}_4}{(2\pi)^3\,2\omega_4}\,2\pi\delta(\omega_3-\omega_4)\,|\mathcal{M}|^2 \quad . \tag{2.28}$$

The usual factor of $(2\pi)^4\delta^{(4)}(p_f-p_i)$ has been substituted with $\delta(E_f-E_i)$ since momentum is not conserved (in fact, the axion momentum is different from the photon momentum, while their energy is the same).

To perform the integral, we choose $\mathbf{k}_3$ to be along $\hat{z}$ and define $x = \cos(\mathbf{k}_4,\mathbf{k}_3)$. In these coordinates, $d^3\mathbf{k}_4 = 2\pi|\mathbf{k}_4|^2 d\mathbf{k}_4 dx = 2\pi\omega_4^2 d\omega_4 dx$ (in the last step we used the fact that the axion is massless and so $|\mathbf{k}_4| = \omega_4$).

Using the δ function to integrate over $d\omega_4$, it follows:

$$\sigma = \frac{1}{8\pi}\int_{-1}^{1}|\mathcal{M}|^2 dx = \frac{(Ze\,g_{a\gamma})^2}{16\pi}\int_{-1}^{1}\frac{|F(\mathbf{q})|^2}{q^4}\,|\mathbf{k}_4\times\mathbf{k}_3|^2\,dx \quad . \tag{2.29}$$

To calculate the cross section, Equation 2.29, we now use the following kinematic relations:

- $|\mathbf{k}_4| = \omega_4 = \omega_3$;
- $|\mathbf{k}_3| = \sqrt{\omega_3^2-\omega_{\rm pl}^2}$;
- $|\mathbf{k}_4\times\mathbf{k}_3|^2 = |\mathbf{k}_4|^2|\mathbf{k}_3|^2\sin^2(\mathbf{k}_4,\mathbf{k}_3) = \omega_3^2\left(\omega_3^2-\omega_{\rm pl}^2\right)(1-x^2)$;
- $|\mathbf{q}|^2 = |\mathbf{k}_4-\mathbf{k}_3|^2 = |\mathbf{k}_4|^2+|\mathbf{k}_3|^2-2x|\mathbf{k}_4||\mathbf{k}_3| = 2\omega_3^2-\omega_{\rm pl}^2-2x\omega_3\sqrt{\omega_3^2-\omega_{\rm pl}^2}$

In these expressions $\omega_{\rm pl}^2 = 4\pi\alpha n_e/m_e$ is the plasma frequency that changes the dispersion relations of the photon in a plasma.

Numerically,

$$\omega_{\rm pl} = 28.7\,{\rm keV}\frac{(\rho_6/\mu_e)^{1/2}}{(1+(1.019\,\rho_6/\mu_e)^{2/3})^{1/4}}\,, \tag{2.30}$$

where $\rho_6 = \rho/10^6\,{\rm g\,cm^{-3}}$ and $\mu_e = \langle A/Z\rangle$

2.4.3 Screening

In the case of screening by non-degenerate electrons, the form factor is:

$$|F(q)|^2 = \frac{|\mathbf{q}^2|}{{\kappa_{\rm nd}}^2 + |\mathbf{q}|^2}\,, \tag{2.31}$$

where ${\kappa_{\rm nd}}^2 = \frac{4\pi\alpha}{T}\sum_j Z_j^2 n_j$ is the inverse Debye length in a non-degenerate plasma. So, the integrand in Eq. 2.29 becomes:

$$\begin{aligned}
&\frac{|F(\mathbf{q})|^2}{q^4}\,|\mathbf{k}_4\times\mathbf{k}_3|^2 = \\
&= \frac{\omega_3^2\left(\omega_3^2-\omega_{\rm pl}^2\right)(1-x^2)}{\left({\kappa_{\rm nd}}^2+2\omega_3^2-\omega_{\rm pl}^2-2x\omega_3\sqrt{\omega_3^2-\omega_{\rm pl}^2}\right)\left(2\omega_3^2-\omega_{\rm pl}^2-2x\omega_3\sqrt{\omega_3^2-\omega_{\rm pl}^2}\right)} = \\
&= \frac{1-x^2}{4\left(\frac{{\kappa_{\rm nd}}^2+2\omega_3^2-\omega_{\rm pl}^2}{\omega_3\sqrt{\omega_3^2-\omega_{\rm pl}^2}}-x\right)\left(\frac{2\omega_3^2-\omega_{\rm pl}^2}{2\omega_3\sqrt{2\omega_3^2-\omega_{\rm pl}^2}}-x\right)} = \\
&= \frac{1-x^2}{4\left(\frac{y_1^2+2y^2-y_0^2}{2y\sqrt{y^2-y_0^2}}-x\right)\left(\frac{2y^2-y_0^2}{2y\sqrt{y^2-y_0^2}}-x\right)} = \\
&= \frac{1-x^2}{4\,(s+r-x)\,(r-x)}\quad,
\end{aligned} \tag{2.32}$$

where we introduced the adimensional quantities: $y = \omega_3/T$, $y_0 = \omega_{\rm pl}/T$ and $y_1 = \kappa_{\rm nd}/T$ and

$$r = \frac{2y^2-y_0^2}{2y\sqrt{y^2-y_0^2}}\,,\qquad s = \frac{y_1^2}{2y\sqrt{y^2-y_0^2}}\,. \tag{2.33}$$

Notice that r and s do not depend on x and so, substituting Equation 2.32 in Equation 2.29, we can compute the cross section analytically:

$$\sigma = \frac{(Ze\,g_{a\gamma})^2}{64\pi} I(y,y_0,y_1)\quad, \tag{2.34}$$

where (see Raffelt & Dearborn 1987)

$$\begin{aligned}
I = \int_{-1}^{1}\frac{1-x^2}{(s+r-x)\,(r-x)}\,dx = \\
\frac{r^2-1}{s}\ln\left(\frac{r-1}{r+1}\right)+\frac{(r+s)^2-1}{s}\ln\left(\frac{s+r+1}{s+r-1}\right)-2\,.
\end{aligned} \tag{2.35}$$

2.4.4 Emission rate (non-degenerate case)

We want to calculate the energy loss by axions in the Primakoff process. This is going to be given by the product of several quantities:

Energy loss = axion energy (ω_4)× number of targets (n_t)× probability of interaction times density of final states ($2\omega_3\sigma$)× photon number density ($\frac{2}{e^{\omega_3/T}-1}$)× density of final states ($\frac{d^3\mathbf{k}_3}{(2\pi)^3\,2\omega_3}$).

Taking into account this, and that to obtain the energy loss per mass we also need to divide by the density, the rate equals:

$$\varepsilon_{\rm nd} = \frac{n_t}{\rho}\int_{\omega_{\rm pl}}^{\infty}\omega_4(2\omega_3\sigma)\left(\frac{2}{e^{\omega_3/T}-1}\right)\frac{d^3\mathbf{k}_3}{(2\pi)^3\,2\omega_3} \tag{2.36}$$

where the subscript "nd" stands for "non-degenerate". We now use $\omega_4=\omega_3$ and $d^3\mathbf{k}_3 = 4\pi{\mathbf{k}_3}^2 d\mathbf{k}_3 = 4\pi\omega_3\sqrt{\omega_3^2-\omega_{\rm pl}^2}\,d\omega_3$ and get

$$\varepsilon_{\rm nd} = \frac{n_t}{\rho\pi^2}\int_{\omega_{\rm pl}}^{\infty}\frac{\omega_3^2\sqrt{\omega_3^2-\omega_{\rm pl}^2}\,\sigma}{e^{\omega_3/T}-1}\,d\omega_3 = \frac{(Z^2n_t)g_{a\gamma}^2\alpha\,T^4}{16\rho\pi^2}\int_{y_0}^{\infty}\frac{y^2\sqrt{y^2-y_0^2}}{e^y-1}\,I\,dy\,. \tag{2.37}$$

After substituting Z^2n_t with the sum $\sum Z_j^2 n_j$, to account for possible different targets, finally we obtain the following formula for the non-degenerate emission:

$$\varepsilon_{\rm nd} = \frac{\alpha g_{a\gamma}^2\,T^4}{4\pi\rho}\left(\sum Z_j^2 n_j\right) f(y_0,y_1) \quad , \tag{2.38}$$

where

$$f(y_0,y_1) = \frac{1}{4\pi}\int_{y_0}^{\infty}\frac{y^2\sqrt{y^2-y_0^2}}{e^y-1}\,I\,dy \quad . \tag{2.39}$$

2.4.5 Numerical considerations

In the following we will use $T_0 = T/{\rm K}$ and $\rho_0 = \rho/({\rm g\,cm^{-3}})$.

If we substitute $\left(\sum Z_j^2 n_j\right) = \frac{\kappa_{\rm nd}T}{4\pi\alpha} = \frac{y_1^2\,T^3}{4\pi\alpha}$ in the above expression for $\varepsilon_{\rm nd}$:

$$\boxed{\varepsilon_{\rm nd} = \frac{g_{a\gamma}^2\,T^7\,y_1^2}{16\pi^2\rho}f(y_0,y_1) \simeq 7.1\times10^{-52}\,g_{10}^2\,\frac{\rm erg}{\rm g\cdot s}\left(\frac{T_0^7}{\rho_0}\right)y_1^2\,f(y_0,y_1)} \quad . \tag{2.40}$$

For the plasma frequency we find, numerically,

$$\boxed{y_0 = \frac{\omega_{\rm pl}}{T} = \frac{3.33\times10^5}{T_0}\frac{(\rho_0/\mu_e)^{1/2}}{(1+(1.019\times10^{-6}\rho_0/\mu_e)^{2/3})^{1/4}}\,.} \tag{2.41}$$

Notice that $\kappa_{\rm nd} \gg \omega_{\rm pl}$ and so $y_1 \gg y_0$. In fact, $\sum Z_j^2 n_j \geq Z_j n_j$ and for the neutrality of the plasma, $\sum_{\rm ions} Z_j n_j = n_e$. Thus,

$$\kappa_{\rm nd}{}^2 = \frac{4\pi\alpha}{T}\sum Z_j^2 n_j \geq \frac{4\pi\alpha}{T} n_e = \omega_{\rm pl}^2 \left(\frac{m_e}{T}\right) \gg \omega_{\rm pl}^2 \tag{2.42}$$

for $T \ll m_e$, which is always the case for us.

It is convenient to separate the contributions of electrons and ions to the screening. In order to do that, κ_{nd} can be written as

$$\kappa_{\rm nd}{}^2 = \kappa_{\rm el}^2 + \kappa_{\rm ions}^2\,, \tag{2.43}$$

with

$$\begin{cases} \kappa_{\rm el}^2 = \frac{4\pi\alpha n_e}{T} = \frac{\omega_{\rm pl}^2 m_e}{T}\,, \\ \kappa_{\rm ions}^2 = \frac{4\pi\alpha \sum Z_j^2 n_j}{T}\,. \end{cases} \tag{2.44}$$

Using the definition of the number density of a given specie

$$n_j = \frac{\rho}{m_u}\frac{X_j}{A_j}\,, \tag{2.45}$$

where $m_u = 1.66 \times 10^{-24}$ g, we can write

$$\kappa_{\rm ions} = \sqrt{\frac{4\pi\alpha\,\rho}{m_u\,T}}\sqrt{\frac{\sum Z_j^2 X_j}{A_j}} \simeq 222\,{\rm eV}\left(\frac{\sum Z_j^2 X_j}{A_j}\right)^{1/2}\left(\frac{\rho_0}{T_8}\right)^{1/2}\,, \tag{2.46}$$

where the sum includes only the ions (not the electrons) contributions. Finally, we collect the results from the screening

$$\boxed{\begin{array}{l} y_1^2 = y_{\rm ions}^2 + y_{\rm el}^2\,, \\ y_{\rm ions} = \frac{\kappa_{\rm ions}}{T} = 2.57\times 10^{10}\left(\frac{\sum_{\rm ions} Z_j^2 X_j}{A_j}\right)^{1/2}\left(\frac{\rho_0}{T_0^3}\right)^{1/2}\,, \\ y_{\rm el} = \frac{\kappa_{\rm el}}{T} = 2.57\times 10^{10}\left(\frac{\sum_{\rm ions} Z_j X_j}{A_j}\right)^{1/2}\left(\frac{\rho_0}{T_0^3}\right)^{1/2}\,, \end{array}} \tag{2.47}$$

where we have used $n_e = \sum_{\rm ions} Z_j n_j$.

Notice that the sum is always only over the ions, even in the case of $y_{\rm e}$. The only difference between $y_{\rm ions}$ and $y_{\rm el}$ is the power of Z_j.

It is also useful to notice that

$$\boxed{y_e = y_0\left(\frac{m_e}{T}\right)^{1/2} = 7.70\times 10^4\, y_0\, T_0^{-1/2}\,.} \tag{2.48}$$

In the case of pure helium chemical composition, like in the stellar cores at the beginning of Horizontal Branch (HB) phase, $\mu_e = 2$, $\left(\frac{\sum_{\rm ions} Z_j^2 X_j}{A_j}\right) = 1$ and $\left(\frac{\sum_{\rm ions} Z_j X_j}{A_j}\right) = 1/2$. Therefore,

$$\begin{cases} y_0 = \frac{0.235\,\rho_4^{1/2}/T_8}{(1+(0.0296\,\rho_4)^{2/3})^{1/4}}\,, \\ \\ y_1 = 3.15\left(\frac{\rho_4}{T_8^3}\right)^{1/2}\,. \end{cases} \tag{2.49}$$

In a plasma, for instance at $T = 10^8$ K and $\rho = 10^4 \mathrm{g\,cm^{-3}}$, y_1 is about 15 times bigger than y_0.

For the axion emission rate, we find

$$\varepsilon_{\rm nd} = 7.1\, g_{10}^2\, \frac{\rm erg}{\rm g\cdot s}\left(\frac{T_8^7}{\rho_4}\right) y_1^2\, f(y_0, y_1)\,. \tag{2.50}$$

At $T = 10^8$K and $\rho = 10^4 \mathrm{g\,cm^{-3}}$, $f(y_0, y_1) \sim 1$ and $y_1^2 \simeq 10$, then (assuming $g_{10} = 1$) $\varepsilon_{\rm nd} \simeq 70\,\mathrm{erg\,g^{-1}\,s^{-1}}$.

2.4.6 Degeneracy

In the case of high density and relatively low temperature one may have to account for possible effects of degeneracy. To measure the degeneracy, one can compare the temperature contribution to the fermion momentum with p_F. In the non-relativistic case, $p^2 = 2mE_{\rm kin}$, where $E_{\rm kin} = E - m$ is the kinetic energy. We can also define $P_T^2 = 2mT$, where T stands for the kinetic energy.

The Fermi momentum is $p_F = (3\pi^2 n)^{1/3}$, where n is the fermion volume density. So, a good way to measure the grade of degeneracy is through the parameter

$$\zeta = \frac{p_F^2}{P_T^2} = \frac{\left(3\pi^2 n\right)^{2/3}}{2mT} \tag{2.51}$$

The non-degenerate case corresponds to large T and low n while the opposite gives the degenerate case. So:

$$\begin{array}{ll} \text{nondegenerate} & \zeta \to 0 \\ \text{degenerate} & \zeta \to \infty \end{array}$$

In order to deal with degeneracy, it is possible to interpolate between the non-degenerate (nd) and the degenerate (deg) in the following way:

$$(1 - w)\varepsilon_{\rm nd} + w\,\varepsilon_{\rm deg}\,. \tag{2.52}$$

Then it holds

$$\begin{array}{lll} \text{nondegenerate} & w \to 0 & (\text{so } \zeta \to 0 \Rightarrow w \to 0)\,, \\ \text{degenerate} & w \to 1 & (\text{so } \zeta \to \infty \Rightarrow w \to 1) \end{array}$$

A suitable choice of w is given by Raffelt & Dearborn (1987):

$$w = \frac{1}{\pi}\arctan(\zeta - 3) + \frac{1}{2}\,. \tag{2.53}$$

Now we have to calculate $\varepsilon_{\rm deg}$ to insert in Equation 2.52. For ions, nothing changes since they are heavy and too non-degenerate for the plasma conditions interesting to us. For the electrons, however, things change in three ways: a) the effective number changes; b) the screening length changes.

The problem with the number of electrons, in principle, can be solved by simply using the procedure in Raffelt & Dearborn (1987), taking into account the Pauli blocking of final states in the case of degenerate electrons as targets. We denote the fraction of degenerate electrons as n_2.

However, it is possible to consider the contribution of the electron number and use $\delta(\mathbf{k}_1 - \mathbf{k}_2)$ to define a reduction factor of the effective number. Then, is possible to define

$$R_{\rm deg} = \frac{\text{num electrons including degeneracy}}{\text{num electrons without considering degeneracy}}\quad . \tag{2.54}$$

Assuming that the momentum of the electrons does not change (which is a good approximation since electrons are much heavier than T), $R_{\rm deg}$ is roughly

$$R_{\rm deg} \simeq \frac{\int d^3\mathbf{k}_1 d^3\mathbf{k}_2 n_1(1-n_2)\delta(\mathbf{k}_1 - \mathbf{k}_2)}{\int d^3\mathbf{k}_1 d^3\mathbf{k}_2 n_1 \delta(\mathbf{k}_1 - \mathbf{k}_2)} \tag{2.55}$$

where $n_i = 1/(\exp(E_i/T - \mu/T) + 1)$. The delta function can be used to eliminate $d^3\mathbf{k}_2$. Let's call $\mathbf{k}_1 = \mathbf{k}$ and $E_1 = E$. In the non-relativistic approximation, $E = m_e + k^2/2m_e$ and so $n = 1/(x^2 - \eta)$, where $x = k/\sqrt{2m_eT}$ and $\eta = (\mu - m_e)/T$.

Using this, it is found.

$$R_{\rm deg} = \int_0^\infty \frac{x^2 e^{x^2-\eta}}{(e^{x^2-\eta}+1)^2}dx \Big/ \int_0^\infty \frac{x^2}{e^{x^2-\eta}+1}\,. \tag{2.56}$$

The η parameter characterizes the stellar degeneracy. In fact, in the case of degeneracy, it holds $\eta \to \zeta$.

For η larger than a few the plasma is degenerate and for $\eta < 0$ it is non-degenerate. In some stellar interiors, namely those of horizontal branch stars, $\eta \simeq -1$, whereas in case of the cores of red giant stars $\eta \simeq 20$ (see, for instance, Raffelt (1996)).

The function $R_{\rm deg}$ is shown in Figure 2.54 (black line). It is equal to 1 for non-degenerate conditions and to zero for very degenerate conditions.

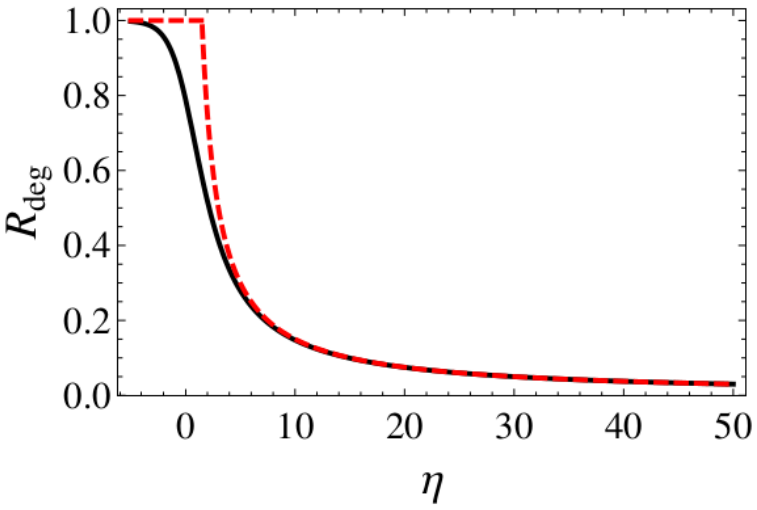

Figure 2.3: The function $R_{\rm deg}$ defined in Eq. 2.54. The black line represents the actual integral while the red, dashed line is the approximation in Eq. 2.66.

Equation 2.54 can be simplified into

$$R_{\rm deg,\ Approx} \simeq \frac{1.5}{\rm Max(1.5, \zeta)} \tag{2.57}$$

Notice that we can substitute ζ with η without making a big error since for $\zeta > 1.5$ the plasma is degenerate enough to have $\zeta \simeq \eta$. The plot is shown in Figure 2.3 (red, dashed line).

For degenerate electrons, the relevant screening momentum is the Thomas-Fermi momentum

$$\kappa^2_{\rm TF} = \frac{4\alpha m_e p_F}{\pi}\,, \tag{2.58}$$

rather than the Debye length. In the above equation, p_F is the Fermi momentum is:

$$p_F = 5.15{\rm keV}\left(\frac{\rho}{\mu_e}\right)^{1/3} = 8.25\times10^{-9}{\rm erg}\left(\frac{\rho}{\mu_e}\right)^{1/3}\,. \tag{2.59}$$

So, in calculating the inverse screening length (and the emission rate) we need to distinguish between ions and electrons:

$$\varepsilon_{\rm deg} = \varepsilon_{\rm ions} + \varepsilon_{\rm el}\,, \tag{2.60}$$

with

$$\boxed{\varepsilon_{\rm ions} = \frac{g_{a\gamma}^2\, T^7\, y_{\rm ions}^2}{16\pi^2\rho} f(y_0, y_{\rm ions})\,, \qquad \varepsilon_{\rm el} = \frac{\alpha g_{a\gamma}^2}{4\pi}\frac{T^4}{\rho}\,(R_{\rm deg}\, n_e)\; f(y_0, y_{\rm TF})\,,} \tag{2.61}$$

where $f(y_0, y_{\rm TF})$ has been defined in 2.39 and

$$y_{\rm TF} = \kappa_{\rm TF}/T\,. \tag{2.62}$$

Notice that the power of ρ and T in $\varepsilon_{\rm el}$ is different with respect to the other ε. That is because there is no y-factor in front of the f in that case. It may be convenient to rewrite $\varepsilon_{\rm el}$ as a form more similar to the other emission rates. We can do that by using $\kappa_{\rm el}^2 = \frac{4\pi\alpha n_e}{T} = \frac{\omega_{\rm pl}^2 m_e}{T}$, solving for n_e and substituting in the above expression for $\varepsilon_{\rm el}$. We find:

$$\varepsilon_{\rm el} = \frac{g_{a\gamma}^2\, T^7\, y_{\rm TF}^2}{16\pi^2\rho}\left(\frac{y_{\rm el}}{y_{\rm TF}}\right)^2 R_{\rm deg}\, f(y_0, y_{\rm ions})\,, \tag{2.63}$$

with

$$\left(\frac{y_{\rm el}}{y_{\rm TF}}\right)^2 = 1.07\, T_8 \left(\frac{\rho_4}{\mu_e}\right)^{-2/3} \tag{2.64}$$

2.4.7 General Formulae

Here we give a set of numerical formulas which can be implemented in the code. The temperature (T) will always be in K and the density (ρ) always in g cm^{-3}.

Numerical Formulas:

For the interpolation:

$$\begin{cases} \zeta = \frac{3.01\times10^5}{T}\left(\frac{\rho}{\mu_e}\right)^{2/3}\,, \\ \\ w = \frac{1}{\pi}\arctan(\zeta - 3) + \frac{1}{2}\,. \end{cases} \tag{2.65}$$

For the electron density:

$$R_{\rm deg} \simeq \frac{1.5}{{\rm Max}(1.5, \zeta)} \tag{2.66}$$

y factors (adimensional):

$$\begin{cases} y_0 = \frac{3.33\times10^5}{T}\frac{(\rho/\mu_e)^{1/2}}{(1+(1.019\times10^{-6}\rho/\mu_e)^{2/3})^{1/4}}\,, \\ y_1 = 2.57\times10^{10}\left[\frac{\sum_{\rm ions}(Z_j^2+Z_j)X_j}{A_j}\right]^{1/2}\left(\frac{\rho_0}{T_0^3}\right)^{1/2}\,, \\ y_{\rm ions} = \frac{\kappa_{\rm ions}}{T} = 2.57\times10^{10}\left(\frac{\sum_{\rm ions}Z_j^2X_j}{A_j}\right)^{1/2}\left(\frac{\rho}{T^3}\right)^{1/2}\,, \\ y_{\rm TF} = \frac{5.74\times10^7}{T}\left(\frac{\rho}{\mu_e}\right)^{1/6}\,. \end{cases} \tag{2.67}$$

Emission rates (in $\frac{\rm erg}{\rm g\cdot s}$)

$$\begin{cases} \varepsilon_{\rm nd} = 7.1\times10^{-52}\,g_{10}^2\left(\frac{T^7}{\rho}\right)y_1^2\,f(y_0,y_1)\,, \\ \varepsilon_{\rm ions} = 7.1\times10^{-52}\,g_{10}^2\left(\frac{T^7}{\rho}\right)y_{\rm ions}^2\,f(y_0,y_{\rm ions})\,, \\ \varepsilon_{\rm el} = 4.7\times10^{-31}\,g_{10}^2\,R_{\rm deg}\left(\frac{T^4}{\mu_e}\right)f(y_0,y_{\rm TF})\,, \\ \varepsilon_{\rm deg} = \varepsilon_{\rm ions}+\varepsilon_{\rm el}\,, \\ \varepsilon_{\rm Tot} = (1-w)\varepsilon_{\rm nd}+w\,\varepsilon_{\rm deg}\,. \end{cases} \tag{2.68}$$

Notice that the power of ρ and T in $\varepsilon_{\rm el}$ is different respect to the other ε. That is because there is no y-factor in front of the f in that case.

The function f can be expressed in terms of the slowly varying function g as:

$$f(y_0,y_*) = \frac{100}{1+y_*^2}\frac{1+y_0^2}{1+e^{y_0}}\,g(y_0,y_*)\,, \tag{2.69}$$

where y_* is y_1 in the case of $\varepsilon_{\rm nd}$, $y_{\rm ions}$ in the case of $\varepsilon_{\rm ions}$, $y_{\rm TF}$ in the case of $\varepsilon_{\rm el}$, while y_0 is always the same. It must be pointed out that y_* appears not only in g but also in the prefactor in Equation 2.69.

Plots of the overall rate we derive for Primakoff process vs density, in case of $g_{10}=1$ and for different temperatures and chemical compositions is shown in Figures 2.4 and 2.5. Both figures shows the decay of the rate at high densities. As it can be seen in Figure 2.4, the higher the temperature the higher is the rate of the process. In addition, the rate is enhanced at low

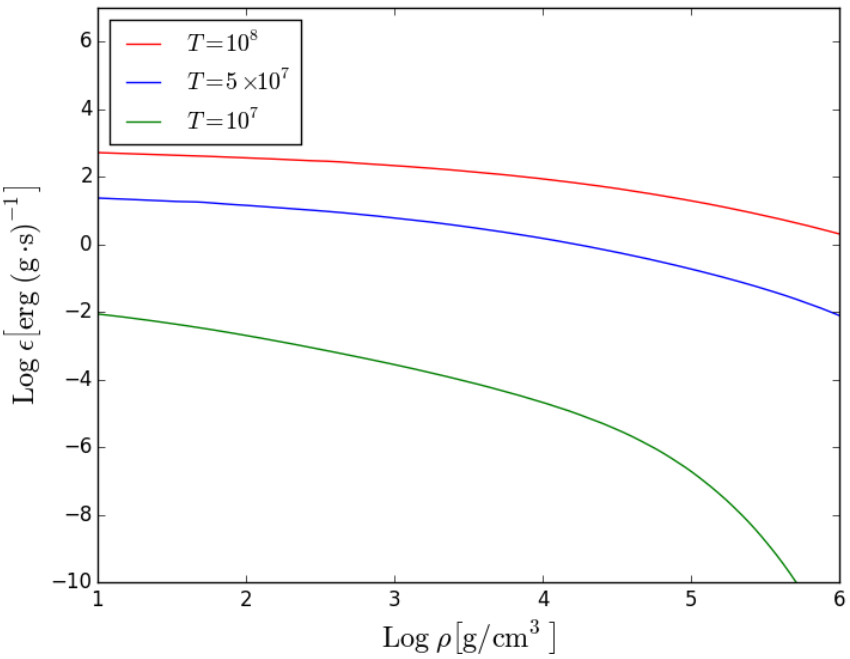

Figure 2.4: Dependence of Primakoff process rate on temperature, in the case of $g_{10} = 1$. Pure helium composition is assumed. The cases of $T = 10^7$, 5×10^7 and 10^8 are shown.

densities for pure carbon plasma with respect to pure helium and helium-carbon mixed plasmas (see Figure 2.5). In contrast, at high densities the effect of degeneracy prevails and the same rate is observed for the three chemical compositions.

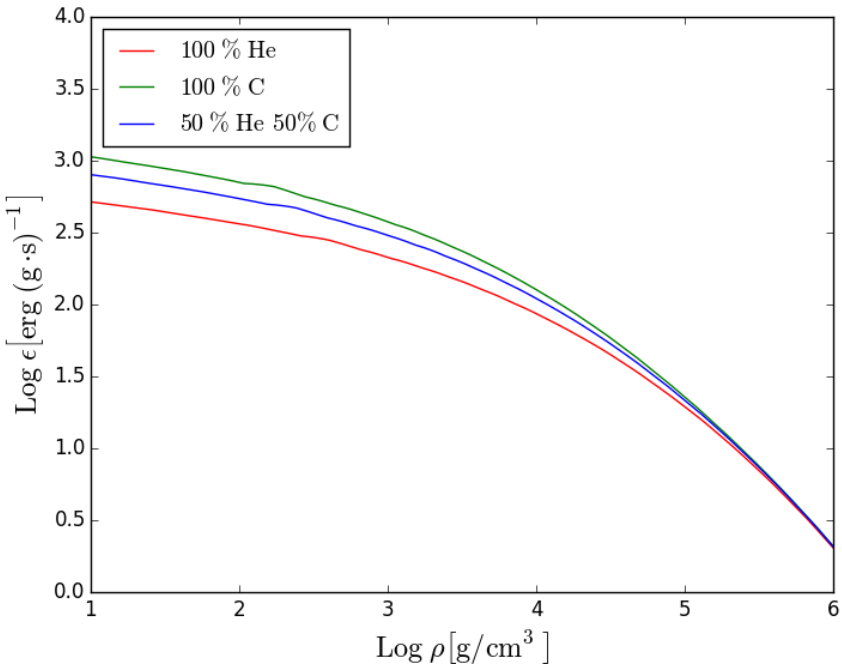

Figure 2.5: Dependence of Primakoff process rate on the chemical composition of the plasma, in the case of $g_{10} = 1$. Pure helium, pure carbon and a 50% mixture of both elements are shown. In all cases $T = 10^8$

Chapter 3

Low mass stars and R parameter

Contents

3.1 Low mass stars evolution

Globular Clusters (GCs) are populations of about 10^6 low mass stars, with an average age of about 13 Gyr and an age difference of $\pm$ 1 Gyr. The metallicities (Z) of GCs range from $2 \cdot 10^{-4}$ to $6 \cdot 10^{-3}$. As stellar formation time is small in comparison with cluster ages, all the stars can be considered the same age. A line of stars with different mass and same age defines an "isochrone" in the Colour-Magnitude Diagram (CMD).

CMDs are the observational counterparts of theoretical luminosity vs effective temperature diagram, where the magnitude is plotted versus colour. In practice, photometric studies of Globular Clusters show points spread around an isochrone (see Figure 3.1). This spread is mainly due to photometric errors and, in some cases, it may hide internal variations of a "second parameter", the first one being the stellar mass (see the review of Gratton et al. (2012)).

The evolution of low mass stars pass through several phases, from the pre-Main Sequence (pre-MS) to the moment it begins to fade away and cools as a white dwarf. The evolutionary track in the theoretical plane of a star of metallicity and mass within GC range (0.82 $M_\odot$, $Z = 10^{-3}$, $Y = 0.248$) can be seen in Figure 3.2. After the pre-MS, a star moves to the HR diagram zone known as Main Sequence (MS), in which the hydrogen core produces energy, burning H into He. Leaving MS, a typical GC star undergoes several transformations and changes the internal conditions and the zones where nuclear reactions take place.

The goal of this dissertation is to use information from the CMDs, or observables directly derived from them, to impose constraints on the fundamental physics. The strain is put on post-MS evolution, when central hydrogen is fully consumed and the temperature in the core rises. In this case the thermal processes producing WISPs are favoured (see section 2.4). In particular we will focus on HB and Red Giant Branch (RGB). The observable we use in our study is the R parameter, which is the number ratio of HB stars and bright RGB stars.

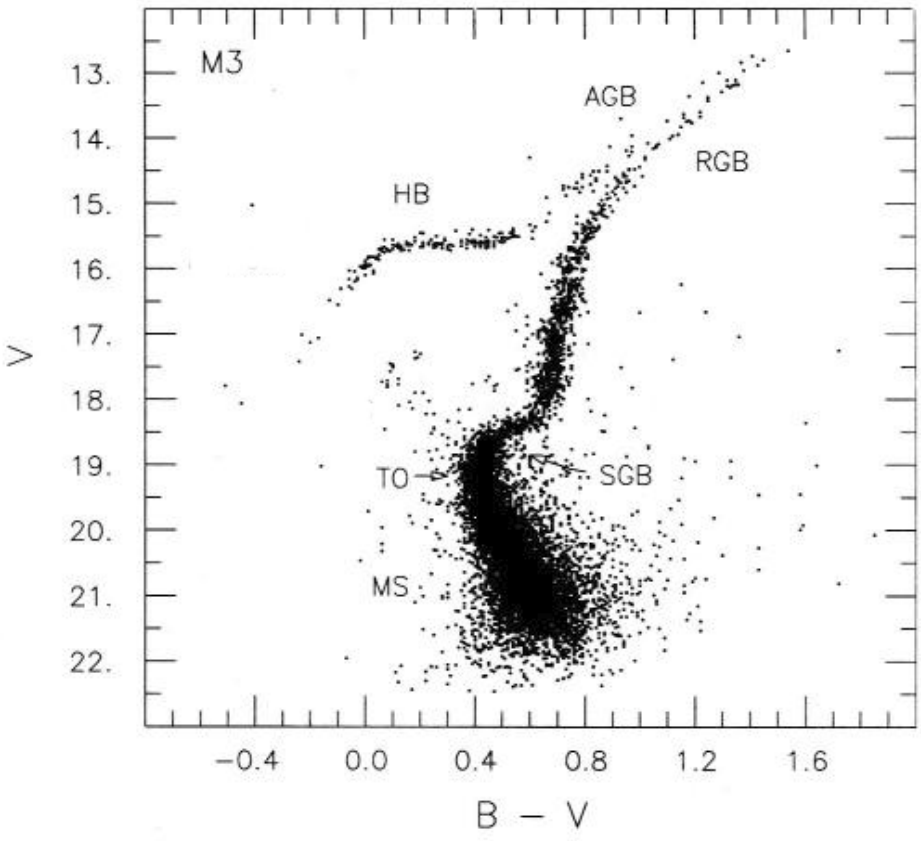

Figure 3.1: Colour-Magnitude diagram of GC M3, adapted from Buonanno et al. (1986). The various evolutionary phases are labeled: MS= Main Sequence, TO = Turn Off, SGB = Sub Giant Branch, RGB = Red Giant Branch, HB = Horizontal Branch, AGB = Asymptotic Giant Branch.

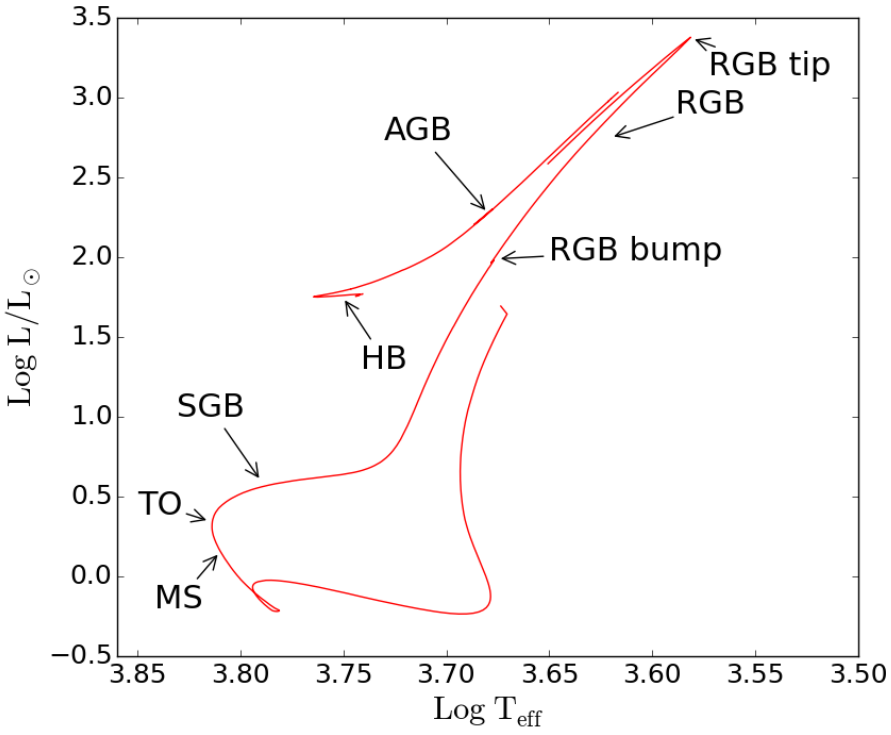

Figure 3.2: Evolution of a low mass, 0.82 $M_\odot$, $Z = 10^{-3}$, $Y = 0.248$ star in the theoretical plane $L/L_\odot$ vs T, computed with FUNS, from ZAMS (zero age main sequence) to AGB. The He flash has been removed. Shown features include Main Sequence (MS), Turn Off (TO), SGB (Sub Giant Branch), RGB (Red Giant Branch), RGB bump and tip, HB (horizontal branch), and Asymptotic Giant Branch (AGB).

3.2 Evolution throughout the RGB phase

3.2.1 The convective envelope

After MS, a low mass star moves to the RGB region, where the effective temperature is lower and the luminosity increases. The internal structure of the star is now a central and dense He core, surrounded by an H shell, where CNO cycle is active and responsible for a high flux of photons outward. As a consequence the entire external envelope (H rich) is unstable against convection. See section (2.3).

The maximum penetration of the convective envelope occurs during the Sub Giant Branch, (SGB). Therefore, the so-called "first dredge-up", a process implying the surface convection zone extending down to the layers where matter has undergone nuclear fusion, takes place. As a result, the fusion products are mixed into the outer layers of the stellar atmosphere where they can appear in the spectrum of the star. In particular, the spectral features of the hydrogen fusion that has occurred is the decrease of the $^{12}C/^{13}C$ and C/N ratios.

The RGB "bump" is a characteristic feature of RGB Luminosity Function. It happens when the hydrogen shell reaches the chemical discontinuity left by the first "dredge up", and the injection of fresh hydrogen into the shell stops the increase of luminosity. In some cases even a decrease of luminosity is expected. The observable consequence is the formation of a bump in the RGB luminosity function of a GC. This feature is clearly evident in Figure 3.3, where the theoretical luminosity vs time of a RGB model with $M = 0.82\,M_{\odot}$, and $Z = 0.001$ is plotted.

3.2.2 The degenerate core

During RGB, the He core density increases up to $\sim 10^6\,\mathrm{g/cm^3}$, so that a large electron degeneracy develops (see Figure 3.4), up to values high enough to cause the core to be dominated by quantum effects and become degenerate. In case of fully degenerate conditions, pressure is independent of temperature, and only controlled by density:

$$P \propto \rho^{\gamma} \quad , \tag{3.1}$$

where $\gamma = 5/3$, in the cases of non relativistic electrons, or $\gamma = 4/3$, in the case of relativistic electrons [1]. Since the core is in hydrostatic equilibrium,

[1] electrons are relativistic when the Fermi energy becomes the order of magnitude of electron rest energy: $\epsilon_F \geq m_e c^2$

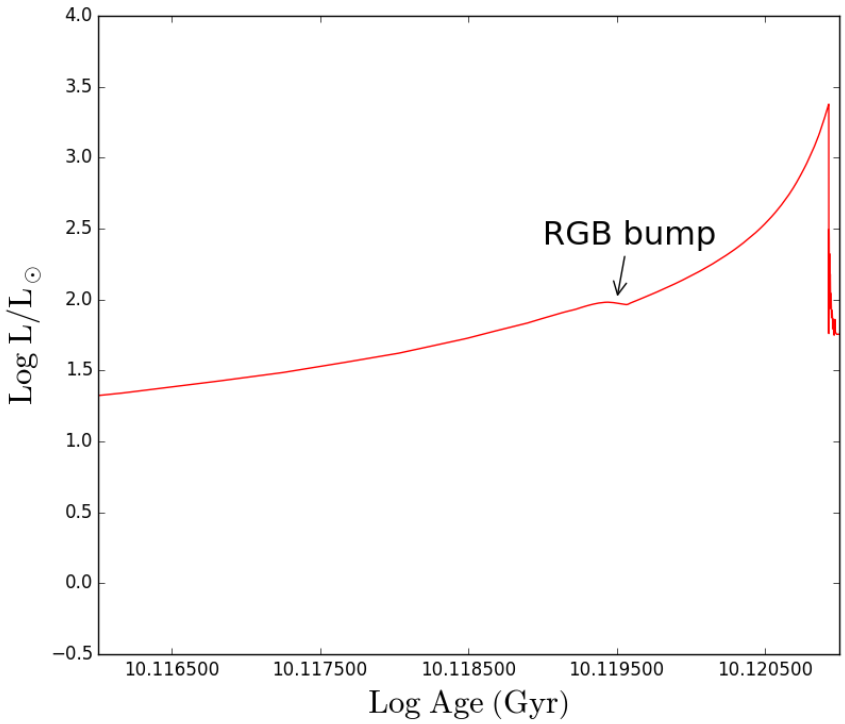

Figure 3.3: Evolution of luminosity, during the RGB phase for a 0.82 $M_\odot$, $Z = 0.001$ stellar model. The arrow indicates the location of the RGB bump.

by combining Equations 3.1 and 2.1, the following relationship between mass and radius in a degenerate core can be derived (see Iben (2013)).

$$M \propto R^{-1/3} \tag{3.2}$$

Note that for a non-degenerate star, R increases as the mass increases. On the contrary in the case of a degenerate core, the relationship between radius and mass is inverted: core mass increases as its radius decreases, because the reduced size squeezes the electron Fermi sea into higher momentum states, providing for increased pressure to balance the increased gravitational force.

The electron degeneracy affects the thermal profile within the core. Indeed, due to the Pauli exclusion principle the electron interactions among themselves, and with ions, are strongly suppressed. In this way the main free path of an electron substantially increases and the conductive energy transport becomes efficient (see section 2.3.2). As a consequence T profile

flattens and the center of the RGB star, and the surrounding layers, get isothermal as is shown in the central panel of Figure 3.5.

3.2.3 Thermal neutrino cooling

The emission of neutrinos is more efficient in evolved stars. Under degenerate conditions, thermal neutrino production is generally suppressed except in the case of plasma neutrinos. In the latter case, the neutrino production rate depends on density. As is shown in Figure 3.4, the density is definitely larger near the center, and in turn in this region the neutrino cooling is more efficient, as can be seen in the lower panel of Figure 3.5. This neutrino cooling produces a decrease of temperature near the center and the maximum temperature is settled more outside (at M $\sim 0.22 M_{\odot}$). Therefore, during the tip, maximum temperature moves to outer layers, as a consequence of energy carried away by neutrinos (see Figure 3.5).

This process could be enhanced if neutrinos had a hypothetical direct electromagnetic interaction, caused by milli-charges or dipole moments. The uncertainties on the hypothetical magnetic dipole moment, μ_ν influence the value of the He core mass attained at the RGB, as well as the luminosity of the RGB tip and HB, as will be discussed in Chapter 4.

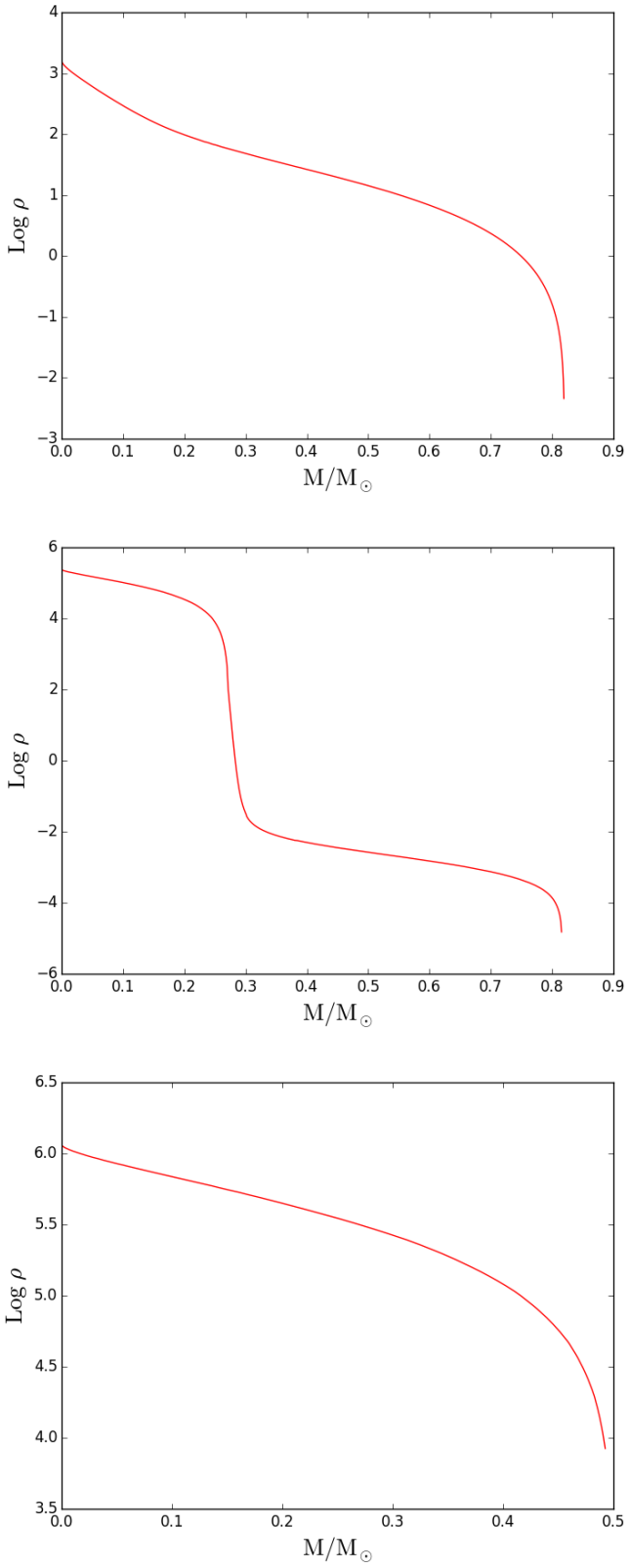

Figure 3.4: Density vs $M/M_{\odot}$ throughout RGB phase. Upper panel corresponds to RGB beginning, middle to the intermediate RGB and lower to the tip region.

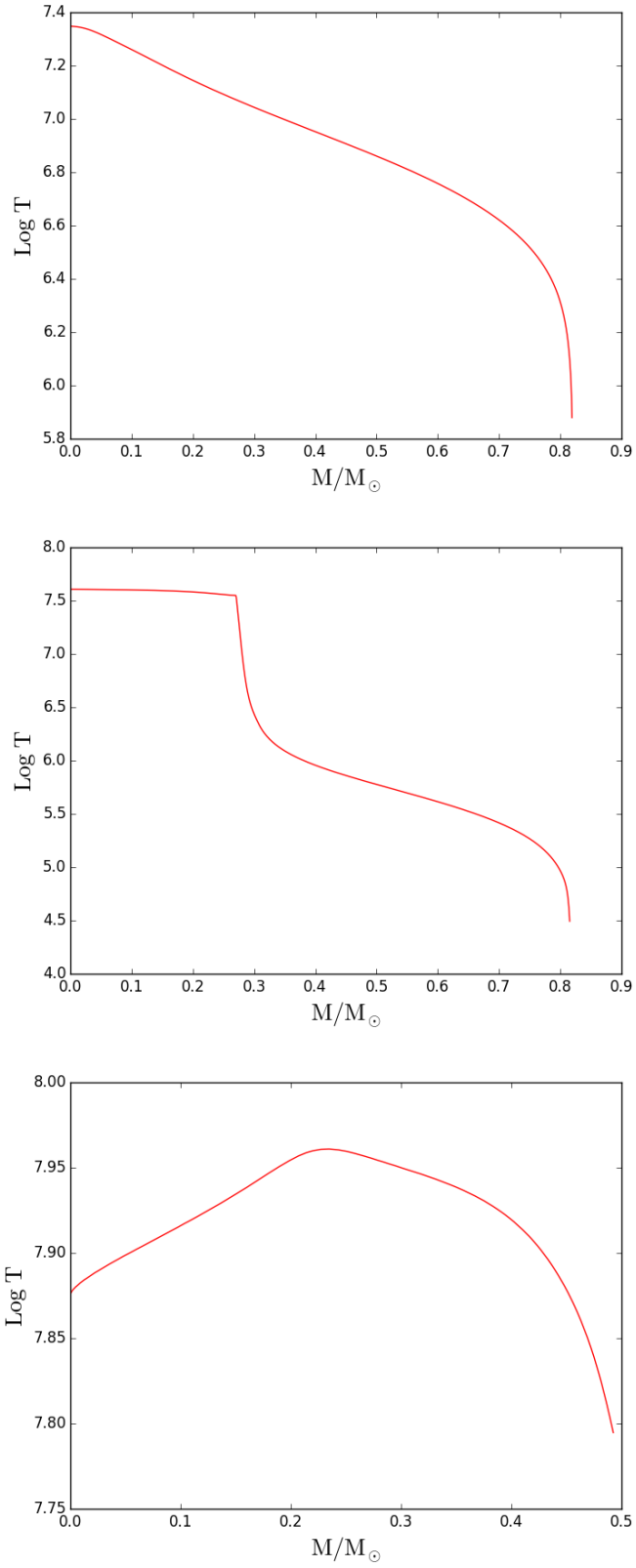

Figure 3.5: Profile of temperature vs $M/M_\odot$ for different times during RGB phase: beginning of the RGB (upper panel), intermediate region (middle panel) and RGB tip (lower panel). Models correspond to a $0.82M_\odot$, $Z = 0.001$, $Y = 0.248$ star.

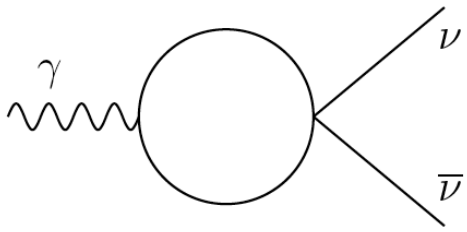

Figure 3.6: Production of neutrino, antineutrino ($\nu\,\bar{\nu}$) pair, by plasma oscillations.

3.3 The He-flash

End of the RGB phase coincides with the He flash. It occurs when a helium core attains a mass of about 0.5 $M_{\odot}$, depending on the chemical composition. Since pressure does not depend on T, but on ρ, because of the degeneracy of the electron component, when the 3α reaction starts, the energy released by the nuclear burning causes an increase of T, but P remains almost unchanged. In other words, the He ignition is not followed by an expansion, as it happens in non-degenerate conditions. The absence of such a feedback leads to the development of a thermonuclear runaway, the helium flash. Obviously, the flash occurs in the layer where the temperature is maximum (see lower panel of Figure 3.5); however, as the temperature increases, the degeneracy is removed and the burning becomes quiescent. Later on conditions for the He ignition are attained in more internal layers, so that a series of flashes are experienced (see Figure 3.7), until a quiescent burning settles in the stellar centre. This moment coincides with the so-called zero horizontal branch (Zero Age Horizontal Branch (ZAHB)).

Before the occurrence of the helium flash, an RGB star is characterized by a large radius ($R \sim 10^2 R_{\odot}$) and it is a rather bright object ($L \sim 3000 \times L_{\odot}$), so that quite a huge mass loss takes place (see section 2.3.8). As a result the mass at the onset of the horizontal branches is significantly reduced with respect to its initial value, the exact value depending on the assumed η parameter.

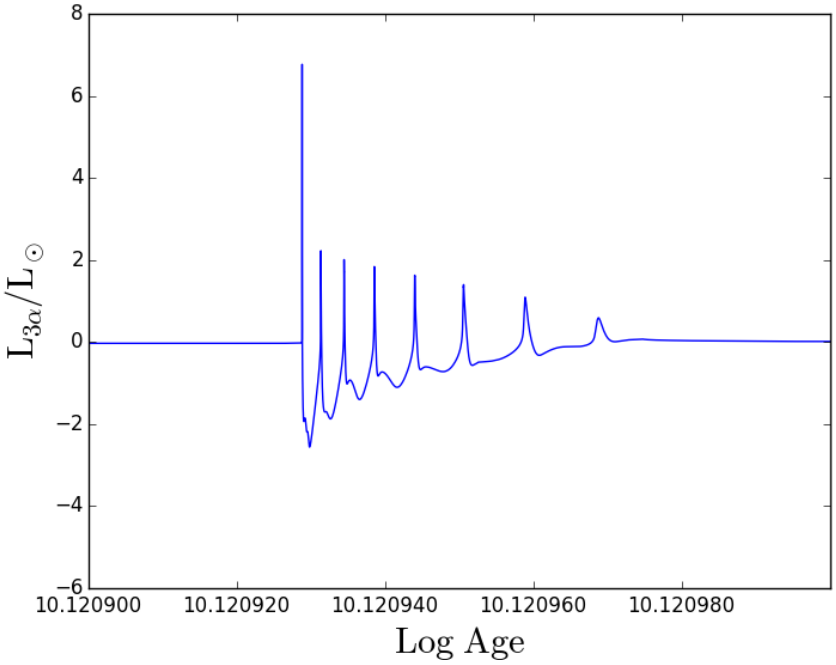

Figure 3.7: He-burning 3α luminosity as a function of time at the epoch of the "He-flash", for a $0.82\,M_\odot$ star, with $Z = 0.001$ and $Y = 0.248$.

3.4 Evolution throughout the HB phase

During the HB the star evolves quietly at an almost constant luminosity. The ZAHB luminosity, essentially depends on the core mass attained at the He flash, while its effective T depends on the current mass and, in turn, on the efficiency of the mass loss occurring during the final part of the RGB. Effectively, the smaller the current mass the hotter the ZAHB. In this way, the observed colour spread of HB stars in GCs is commonly interpreted as a star-to-star variation of the efficiency of the mass loss during the RGB, or, equivalently, as a variation of the η parameter.

3.4.1 The competition between the 3α and the $^{12}C\,(\alpha,\gamma)^{16}\,O$ processes

During HB phase H burning takes place at the base of the H-rich envelope, while He burning occurs near the centre. Initially the 3α reactions provide the major contribution to the nuclear energy release. Once a suitable amount of ^{12}C is accumulated, the $^{12}C\,(\alpha,\gamma)^{16}\,O$ starts to compete with the 3α. Due to the fact that 3α requires three helium nuclei instead of the only one needed in case of $^{12}C\,(\alpha,\gamma)^{16}\,O$, and that almost the same energy is pro-

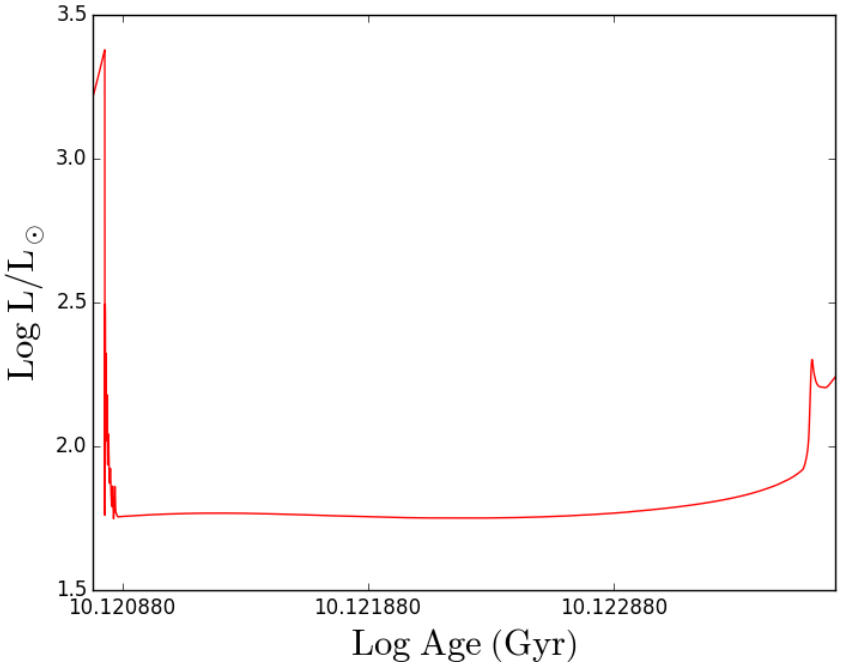

Figure 3.8: Luminosity vs t during HB phase for a 0.82 $M_{\odot}$ star. The ZAHB mass is 0.68 $M_{\odot}$. The two extreme luminosity peaks coincide with the RGB tip and the onset of the AGB.

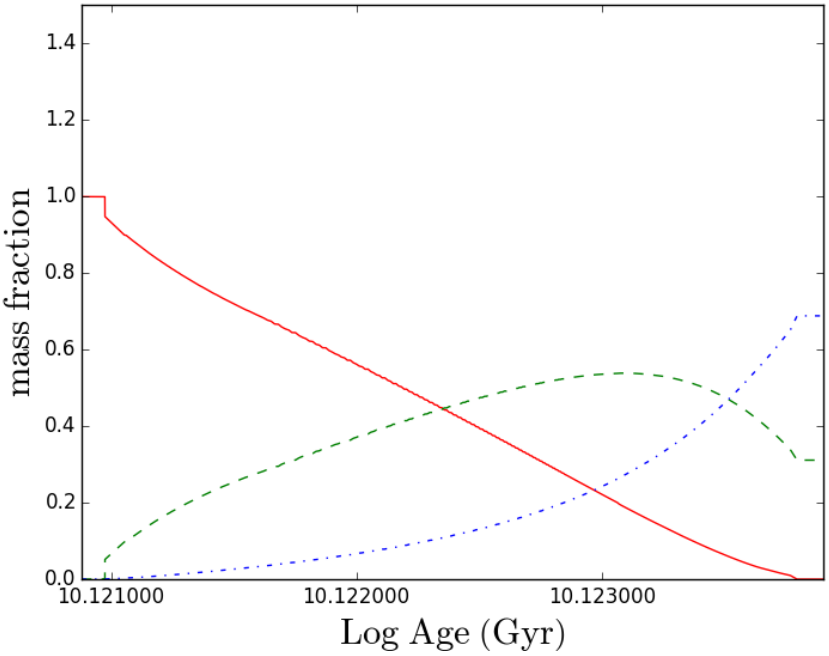

Figure 3.9: Evolution of ^{4}He (red solid line), ^{12}C (green dashed line), ^{16}O (dashed point) central mass fractions during HB phase for a 0.82 $M_{\odot}$ star ($Z = 0.001$, $Y = 0.248$).

duced by the two reactions (of about 7 MeV), the onset of the $^{12}C\,(\alpha,\gamma)^{16}\,O$ process enlarges the duration of the HB phases. During the final part of the core helium burning, when the helium mass fraction decreases below ~ 0.1 the reaction $^{12}C\,(\alpha,\gamma)^{16}\,O$ becomes the dominant process.

The chemical evolution during the HB phase is shown in Figure 3.9. The uncertainties of the aforementioned nuclear reactions have an important influence on the time a star lasts in the HB phase. The effect of these uncertainties will be discussed in Chapter 4.

3.4.2 Convective core and semiconvection

As stated before in Chapter 2, due to the induced overshoot, convective core grows and a semiconvective layer develops. Semiconvection naturally arises in a zone just outside the fully convective core of an He burning star. In this zone, which is initially dynamically unstable, the ingestion of fresh He from outside causes a decrease of the opacity and, in turn, a decrease of the radiative gradient. Therefore a negative feedback on that limit precludes

further mixing. As a result, mixing regulates itself in such a way that in the whole semiconvective layer the marginal stability condition,$\nabla_{rad} = \nabla_{ad}$ holds (see also section 2.3.7)

However, if a substantial mechanical overshoot occurs at the external border of the fully-convective core, the semiconvective layer is engulfed and, then, cancelled. Anyway a significant overshoot is excluded on the base of several observational constraints (Straniero et al. 2003).

3.5 The R parameter, R

From an observational point of view, R parameter is defined as the number ratio of HB and "upper RGB" stars. The latter are the RGB stars with a V magnitude brighter than that of the so-called ZAHB line, which is commonly taken at log $T_{\rm eff} = 3.85$, which corresponds roughly to B-V colour between 0.2-0.6 :

$$R_{obs} = \frac{N_{HB}}{N_{\rm upper\ RGB}} \quad . \tag{3.3}$$

From a theoretical point of view, R parameter is the ratio of the times spent by a star in the HB and upper RGB phases (in the following t_{HB} and t_{RGB}). Thus the following definition also holds:

$$R_{th} = \frac{t_{HB}}{t_{RGB}} \quad . \tag{3.4}$$

The equivalence between Equations 3.3 and 3.4 is guaranteed by the fact that the number of stars observed in a given evolutionary phase is proportional to the time spent by the star in the same phase.

The R parameter is relevant in many stellar evolution studies. It was introduced initially as a way of measuring the helium content in stellar populations, more specifically, Galactic GCs (Iben 1968; Iben & Rood 1969). In this dissertation we look for new physics which could have an effect on it, following previous claims that additional energy sinks related to axion emission in low mass stars can modify the R parameter by affecting the evolution of HB (Raffelt & Dearborn 1987).

3.5.1 The theoretical R parameter

In this section the theoretical R parameter, R_{th} is determined from stellar models. To allow a comparison of theoretical and observed R parameter, we must work in the so-called "observative plane", whose variables are V mag

Table 3.1: V mag at ZAHB, HB and RGB lifetimes, and interpolated values to Log T_{eff} = 3.85 of models with $\eta = 0.20$ and $\eta = 0.35$. In both cases mass, Y, and Z are the same ($0.82\,M_{\odot}$, $Y = 0.248$, $Z = 0.001$).

η	Log T_{eff}	V_{ZAHB}	t_{HB} (Myr)	t_{RGB} (Myr)
0.20	3.7410	0.60944	86.3882	61.1258
0.35	3.94775	0.60949	89.8834	61.3093
Interpolation at Log T_{eff} = 3.85	3.8500	0.60946	88.23068	61.2225

Table 3.2: Effects of helium initial content, Y, on R_{th}

Y	R
0.230	1.32
0.240	1.38
0.248	1.44
0.262	1.52

and B-V colour, and therefore the values of $L/L_{\odot}$ given by FUNS must be converted into V magnitude values. In order to transform these luminosities into V magnitude we use bolometric corrections computed by Castelli & Kurucz (2004).

Mass loss plays an important role in our calculations. The larger the mass loss is, the smaller the residual envelope mass when the helium ignition becomes and then T_{eff} at ZAHB is higher. According to classical definition of R parameter, V mag at ZAHB, must be taken at Log T_{eff} = 3.85, but tracks with different mass loss parameters, η, have different ZAHB temperatures. In order to handle this problem, we compute tracks with the same initial mass ($0.82\,M_{\odot}$), metallicity (0.001) and helium mass fraction ($Y = 0.248$), but different values of η, namely $\eta = 0.2$ and $\eta = 0.35$, and interpolate the lifetimes and V mag to Log T_{eff} = 3.85.

An example of this procedure is shown in Table 3.1. Therefore, from the corresponding interpolated lifetimes, it is possible to calculate R_{th}.

Using data of Table 3.1, we obtain a value, $R_{th} = 1.44$. As already recalled, this results depend on the assumed helium abundance. Therefore, we should calculate the relationship between R_{th} and Y, computing several models with different Y values. The results are reported in Table 3.2 and Figure 3.12. Note that R_{th} linearly depends on Y.

The dependence of R_{th} on metallicity, Z, between 0.0003 and 0.001 has also been tested. Similarly, we have investigated the effect of a variation of stellar mass, by computing models with $M = 0.84$ and $M = 0.82$, which

Table 3.3: Effect of Z and M on R_{th}

$M/M_\odot$	Z	Y	R_{th}
0.84	0.001	0.248	1.441
0.82	0.0003	0.248	1.438

corresponds to an age variation between 11.1 and 13.3 Gyr. The results are reported in Table 3.3. We found, as expected, negligible variations of R_{th} with M and Z.

3.5.2 The observed R parameter

The large amount of new photometric studies of GCs accumulated over the last 20 years by exploiting Earth and space based telescopes allows a more accurate determination of the R parameter. In this dissertation we use the data of Salaris et al. (2004), who reported measurements of a sample of 57 galactic clusters. We consider a subsample of 39 GCS of this catalog, with total metallicity [Fe/H]< -1.1. The data of this subsample are shown in Table 3.4, and Figure 3.11. Although in the mentioned range R does not depend on metallicity, this statement does not hold for higher values of Z. At larger metallicity, namely values of $[Fe/H]$ higher than -1, the RGB bump is too faint to enter into the RGB star count and, in turn, the resulting R is definitely larger, as can be seen in Figure 3.10. Therefore, in order to compare with observational data, we will consider only GCs where $[Fe/H] < -1.1$, using the standard spectroscopic notation for the relative abundances, [M/H]$= \log_{10}(\mathrm{Z/X}) - \log_{10}(\mathrm{Z/X})_\odot$.

We calculate a weighted mean of the R parameters reported in Table 3.4. To do that, we use the values of σ from this table and define a weight, ω_i, which is the inverse of the error of each observed R parameter, $\omega_i = \frac{1}{\sigma_i}$. Then, the weighted mean is

$$\bar{R} = \frac{\sum_i^N \omega_i \cdot R_i}{\sum_i^N \omega_i} = \frac{\sum_i^N \frac{1}{\sigma_i} \cdot R_i}{\sum_i^N \frac{1}{\sigma_i}} \quad , \tag{3.5}$$

where the sum extend over the 39 GCs of the sample. Taking into account that the square of the standard deviation of a weighted mean satisfies

$$s^2 = \frac{1}{\sum_i^N \omega_i^2} = \frac{1}{\sum_i^N \frac{1}{\sigma_i^2}} \quad , \tag{3.6}$$

using Equations 3.5 and 3.6 we find the following mean value and error

$$\bar{R} = 1.39 \pm 0.03 \quad , \tag{3.7}$$

Table 3.4: Subsample of clusters with $[M/H] \leq -1.1$, taken from Salaris et al. (2004). R parameter and the corresponding errors $\sigma(R)$, as well as metallicity and the HB type parameter (see the text) are shown.

GGC	$[Fe/H]_{CG97}$	R parameter	$\sigma(R)$	HB_{type}
IC 4499	-1.27	1.351	0.302	0.11
NGC 362	-1.15	1.358	0.193	-0.87
NGC 1261	-1.10	1.208	0.170	-0.71
NGC 1851	-1.14	1.457	0.163	-0.36
NGC 1904	-1.37	2.055	0.251	0.89
NGC 2808	-1.15	1.598	0.139	-0.49
NGC 3201	-1.15	1.136	0.319	0.08
NGC 4147	-1.59	1.767	0.408	0.55
NGC 4372	-1.94	1.111	0.366	1.00
NGC 4590	-1.99	0.854	0.200	0.17
NGC 4833	-1.58	2.189	0.405	0.93
NGC 5024	-1.89	1.477	0.159	0.81
NGC 5634	-1.61	1.433	0.184	0.91
NGC 5694	-1.15	1.537	0.167	0.71
NGC 5824	-1.67	1.415	0.092	0.79
NGC 5904	-1.11	1.194	0.146	0.31
NGC 5946	-1.15	1.321	0.171	0.71
NGC 5986	-1.44	1.423	0.144	0.97
NGC 6093	-1.44	1.031	0.144	0.97
NGC 6139	-1.42	1.244	0.121	0.91
NGC 6205	-1.39	1.719	0.197	0.97
NGC 6218	-1.37	1.366	0.292	0.97
NGC 6229	-1.30	1.485	0.140	0.24
NGC 6235	-1.17	0.949	0.218	0.89
NGC 6273	-1.45	1.554	0.136	0.97
NGC 6284	-1.17	1.210	0.157	0.83
NGC 6287	-1.90	1.519	0.273	0.98
NGC 6293	-1.73	1.351	0.190	0.90
NGC 6522	-1.21	1.183	0.159	0.71
NGC 6544	-1.31	1.500	0.395	1.00
NGC 6584	-1.30	1.217	0.235	-0.15
NGC 6681	-1.27	1.755	0.283	0.96
NGC 6717	-1.10	0.722	0.267	0.98
NGC 6864	-1.10	1.712	0.194	-0.07
NGC 6934	-1.30	1.621	0.218	0.25
NGC 6981	-1.30	1.088	0.205	0.14
NGC 7078	-2.12	1.883	0.175	0.67
NGC 7089	-1.39	1.455	0.183	0.96
NGC 7099	-1.91	2.607	0.531	0.89

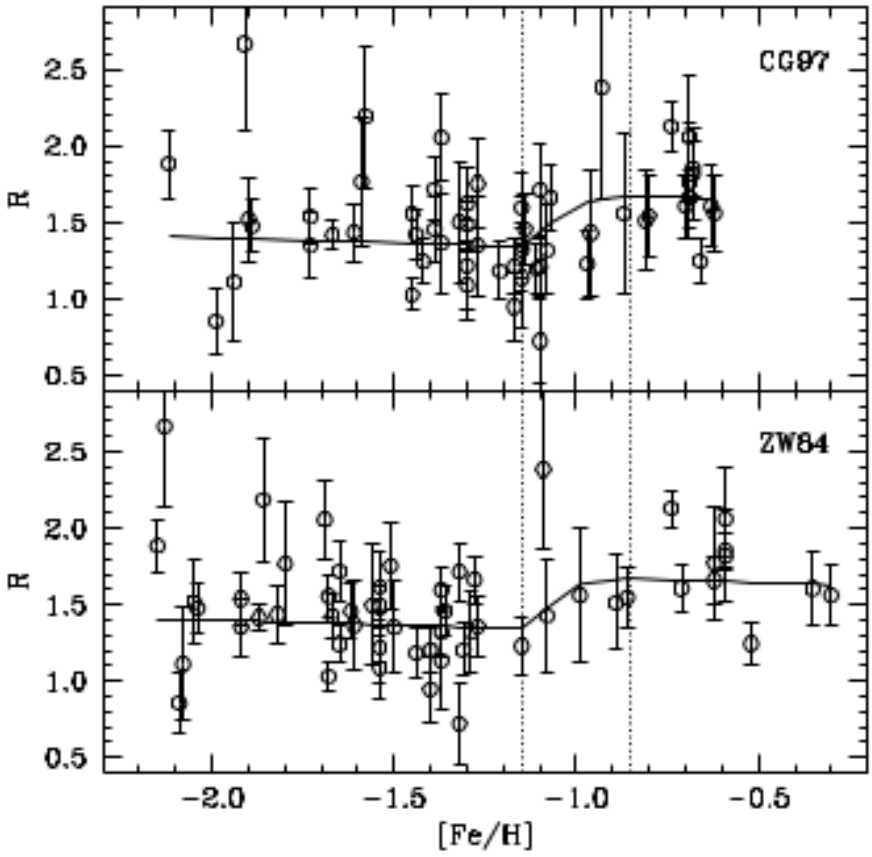

Figure 3.10: In the case of a large metallicity GC, the bump is much too faint and falls down the ZAHB, causing a bias in R_{obs} parameter determination. Plot taken from Salaris et al. (2004).

In the following, we will take the latter as the value of the observed R parameter, R_{obs}.

Some GCs are believed to harbor He enhanced stellar populations. As the presence of these He-rich stars would lead to a certain overstimation of R_{obs} parameter, we have to quantify this effect and exclude GCs where hints of He enhancement exist. Due to the fact He enhanced stars are less massive than coeval stars with primordial He content, the external layers outside the He core become thinner during the HB phase and the T_{eff} rises to higher values, which implies the stars locate in the bluer part of the HB region. We define the HB_{type} parameter of Table 3.4 in Equation 3.8

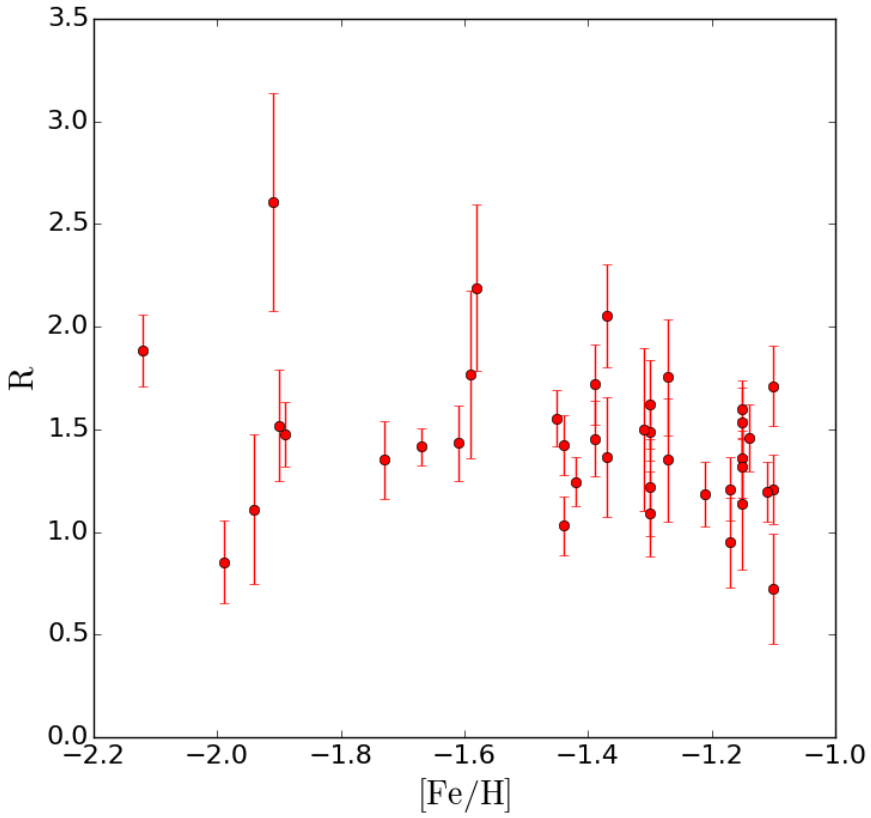

Figure 3.11: Observed R parameter vs $[Fe/H]$, for a subsample of 39 GCs from Salaris et al. (2004).

$$HB_{type} = \frac{n_B - n_V}{n_B + n_V + n_R} \quad , \tag{3.8}$$

where n_B, n_V and n_R are the number of stars "bluer" than the RR Lyrae instability strip stars (or with a hotter surface temperature), within the strip, and redder (with cooler surface temperature) than the instability strip stars, respectively. To exclude the possible He-enhanced GCs we impose the criterion

$$HB_{type} < 0.8 \quad , \tag{3.9}$$

and calculate again the value of R_{obs}. The result is $R_{obs} = 1.39 \pm 0.04$. This coincides with the one obtained for the whole sample, supporting the usual assumption that the bulk of the stars in the GCs sample has the same He abundance.

3.5.3 The predicted R parameter and Y

As stated before, the R parameter has been used to determine the helium mass fraction, Y. Discrepancies between the predicted values of Y, calculated by means of a calibration of R_{th} vs Y, and the observational measurements of helium mass fraction, could indicate:

- Systematic errors on Y determination;
- Uncertainties on R_{th} parameter due to SM physics, namely the aforementioned magnetic dipole moment of the neutrino;
- New Physics affecting lifetimes, for instance, the axion or other BSM particles.

The fit of R_{th}, calculated in our models, vs Y is shown in Figure 3.12. Recent observational measurements of Y are those made by Izotov et al. (2013) and Aver et al. (2013). Both are pretty similar, and we choose Aver data on the bases we discuss in Chapter 4. This value is Y = 0.2535 ± 0.0036 (1σ)

By means of the linear relation shown in 3.12, for the average value of R_{obs} we found $Y = 0.2406$, which seems to indicate some mismatch between theory and experiment, suggesting the possible need of new physics.

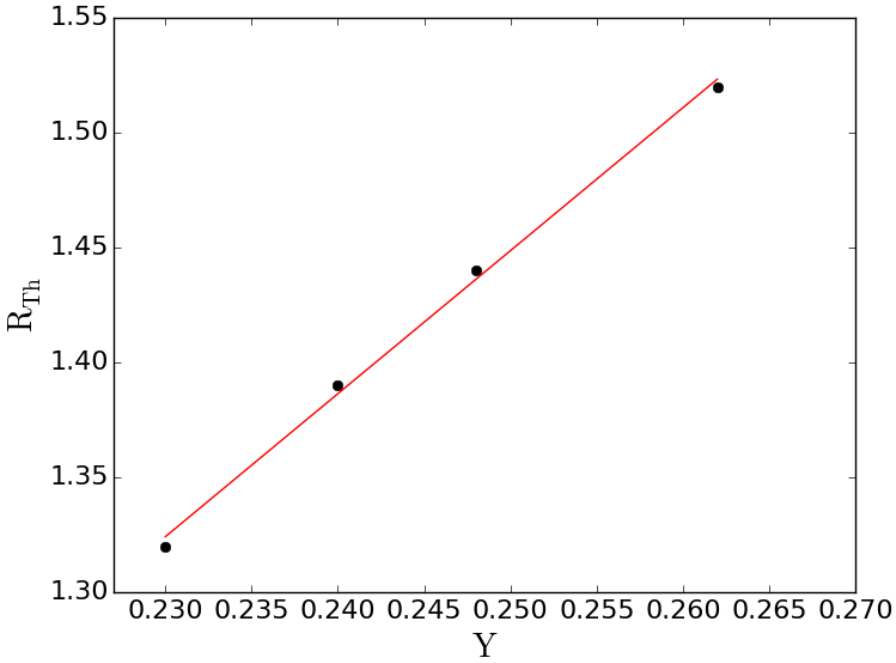

Figure 3.12: Fit of R_{th} with respect to the initial helium mass fraction, Y.

Chapter 4

Bound on Axions from stellar evolution

Contents

4.1 Introduction

In this chapter we investigate the possibility of axion-like particles (ALPs) production inside the cores of HB and RGB stars, whose temperature at the center is around 10^8 K, high enough to allow the production of particles of masses up to a few keV. As stated in Chapter 3, our approach is based on an accurate simulation of the theoretical R parameter, R_{th}, the number ratio of HB and RGB stars brighter than ZAHB, and in the previous hint of the necessity of an additional energy sink to explain the mismatch between R_{th} and the observations (see section 3.5.3).

In order to obtain theoretical values of the R parameter we compute low mass stellar models from the pre-MS to the beginning of the Asymptotic Giant Branch (AGB) phase. We look into the effects of axion-photon coupling ($g_{a\gamma}$) and obtain a theoretical function which relates R with helium initial mass content, Y, and $g_{a\gamma}$.

A study of energy losses in the models with different values of coupling constant, $g_{a\gamma}$, is performed to quantify the effect of axions on RGB and HB phases. Comparison of R_{th} and R_{obs} enables the imposition of constraints on $g_{a\gamma}$.

The advantage of using the R_{obs} parameter derived from observations of GC is that it is not affected by systematic uncertainties such as those due to the distance of the cluster, photometric calibration or metallicity.

4.2 Analysis

It was recognized long ago (Iben 1968; Iben & Rood 1969; Buzzoni et al. 1983) that the R parameter is sensitive to the helium mass fraction. In context of the axion bounds this dependence has so far been neglected. Indeed, even a considerable decrease of the HB lifetime caused by a large value of $g_{a\gamma}$ could be compensated by a suitable increase of the assumed He content, which would produce a higher t_{HB}, masking R parameter variation due to axion effects on HB lifetimes.

Because of this degeneracy between the hypothetical effects of new physics and helium content, a proper evaluation of the axion constraints from the R parameter relies on our knowledge of the He abundance in the GCs.

Measurements of helium abundance in GCs stars are challenging due to the low temperature of their atmospheres. Indeed, ultraviolet data are

Table 4.1: Observations of primordial helium mass fraction, Y_p.

Observable	References	Mean value	1σ
Helium content, Y_p	Aver et al, 2013	0.2535	0.0036
Helium content, Y_p	Izotov et al, 2013	0.255	0.003

needed to perform He abundance analysis in stars, and these spectroscopic windows are not achievable from Earth. In addition, convection, rotationally induced mixing, and other secular phenomena, such as gravitational settling, modify the He abundance in the atmospheres of these stars. For this reason, the primordial He (Y_p) is often adopted for GCs stars, since they are among the first stars that appeared in the Universe. In the last 20 years, Y_p has improved significantly, changing from ~ 0.23 (Olive & Steigman 1995) to ~ 0.25 (Izotov et al. 2013).

The most recent measurements of Y_p are those reported by Izotov et al. (2013) and Aver et al. (2013) (see Table 4.1). These two groups use similar procedures and tools, but different datasets. In particular, Aver et al. (2013) use high accuracy spectra of 16 Blue Compact Dwarf Galaxies with $1.5 < \mathrm{O/H}(\times 10^5) < 13$. This range of O/H is approximately the same as that found in the 39 GCs we used to derive the R_{obs} parameter. The 111 $\mathrm{H_{II}}$ regions used by Izotov et al. (2013) extend to larger metallicity, even though most of them have O/H in the same range as Aver et al. (2013).

In spite of the different datasets, the resulting weighted average values for the He abundance are quite similar, namely: $Y = 0.2535 \pm 0.0036$ and 0.255 ± 0.003 for Aver et al. (2013) and Izotov et al. (2013), respectively.

Since the result obtained by Izotov et al. (2013) could be slightly higher, because of the few high Z $\mathrm{H_{II}}$ regions included in their dataset, in the following we will use the weighted average value reported by Aver et al. (2013) for the same metallicity range of the 39 GCs of our sample.

The invariance of R parameter with respect to metallicity and mass, checked previously, ensures that we can expect that a $0.82\, M/M_{\odot}$, $Z = 0.001$ model, reproduces well the evolutive tracks of the stars in a GC. We have computed several models, varying the Y between 0.23 and 0.29 and the axion-photon, g_{10} between 0 and 1. R_{th} is calculated as described in Chapter 3. The energy loss has been calculated as described in Section 2.4.

An analysis of main characteristics of the model enables an interpretation of the effects of axions along RGB and HB phases. From the theoretical rate derived in Chapter 2, we expect a more important influence along HB,

Table 4.2: Axion effects on HR diagram at RGB and early HB phases and helium core mass at flash, M_{HeC}. Models are calculated for a Reimers parameter $\eta = 0.2$. In all the cases, initial mass, helium mass fraction and metallicities are $0.82\,M_{\odot}$, $Y = 0.248$ and $Z = 0.001$.

g_{10}	Log $L/L_{\odot}$ at tip	Log $L/L_{\odot}$ at bump	Log $L/L_{\odot}$ at ZAHB	$M_{HeC}/M_{\odot}$
0.00	3.377	1.981	1.751	0.502
0.30	3.382	1.965	1.752	0.503
0.50	3.389	1.983	1.753	0.504
0.75	3.404	1.985	1.756	0.507
1.00	3.423	1.988	1.758	0.511

Table 4.3: Axion effects on the central temperature and density at RGB tip and the central temperature at the ending of HB phase. In all models, η has the same value ($\eta = 0.2$). Mass, helium mass fraction and metallicities are $0.82\,M_{\odot}$, $Y = 0.248$ and $Z = 0.001$

g_{10}	Log T_C^{Tip}	Log ρ_C^{Tip}	Log $T_C^{\text{HB end}}$
0.00	7.876	6.058	8.286
0.30	7.876	6.061	8.285
0.50	7.875	6.066	8.286
0.75	7.876	6.075	8.292
1.00	7.876	6.087	8.299

because of the higher temperature and lower density with respect to RGB.

Variations of luminosities at tip, and ZAHB are negligible, as is shown in Table 4.2. In the case of the model with the higher coupling constant, $g_{10} = 1.0$, log $L/L_{\odot}$ of the RGB tip increases only 1.32 %, with respect to the reference model. In addition there are only slight variations of the mass of the helium core at the He-flash, as can be seen in Table 4.2 and, neither changes of central temperature nor central density at RGB tip are significant when g_{10} is increased, (see Table 4.3). The profile of T vs $M/M_{\odot}$ does not change significantly, for models with different $g_{a\gamma}$ at the tip (see Figure 4.1).

Evolution of ^4He, ^{12}C, and ^{16}O mass fractions during the core He burning phase is shown in Figure 4.2, for models with different g_{10}. The final mass fractions are similar, whereas HB lifetimes change appreciably: the higher g_{10}, the faster the He burning. Therefore an increase of g_{10} implies a shorter t_{HB} and then a lower R parameter. The effect of g_{10} on lifetimes is also shown in Figure 4.3 where the faster evolution of luminosity along HB is evident when $g_{10} > 0$.

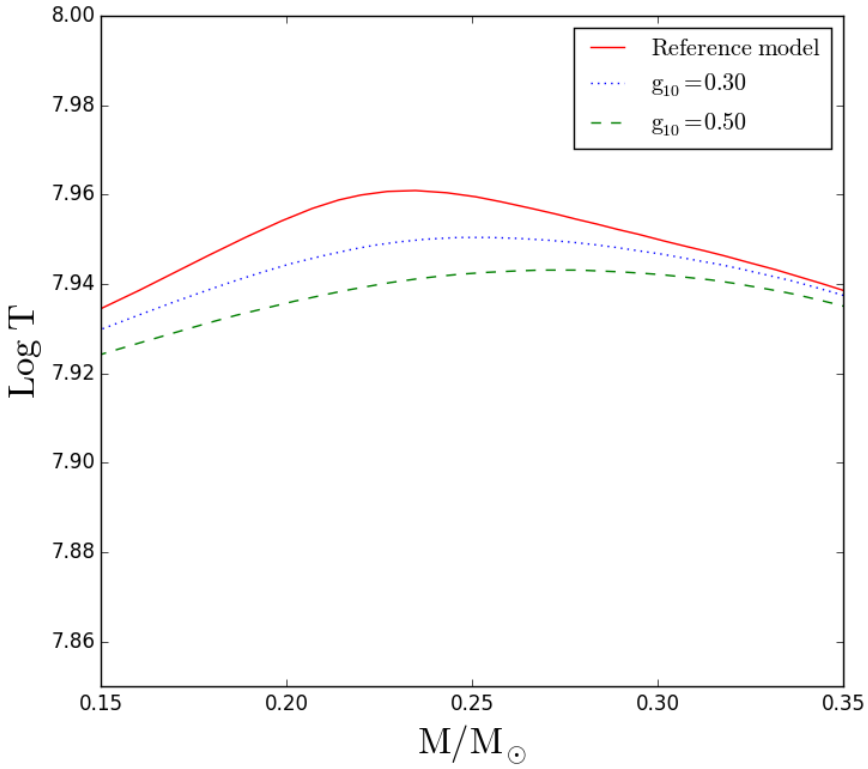

Figure 4.1: Profile of T vs mass coordinate, $M/M_{\odot}$, for a reference model without axion (red solid line), and axion models with $g_{10} = 0.30$ (blue dotted line), and $g_{10} = 0.50$ (green dashed line).

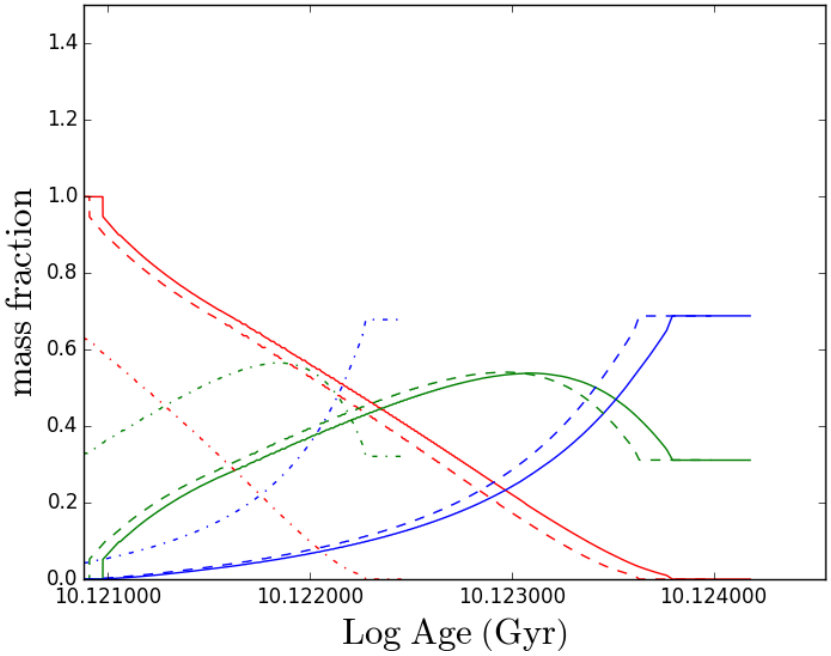

Figure 4.2: Evolution of central ^4He (red), ^{12}C (green), and ^{16}O (blue) mass fractions, for the reference model without axions (solid line), $g_{10} = 0.30$ (dashed line), and $g_{10} = 1.00$ (dashed and dotted line). In all cases, $M = 0.82 M_\odot$, $Y = 0.248$, and $Z = 0.001$.

The HB lifetime, t_{HB}, and the computed R parameter for different $g_{a\gamma}$ values are shown in Table 4.4. The reduction of R parameter for increasing values of g_{10} is evident.

In order to quantify the effect of $g_{a\gamma}$ and Y on R parameter, simulations varying the initial He content and $g_{a\gamma}$ were accomplished. The resulting R_{th} is shown in Table 4.5. We find it is possible to derive a relationship which fits the predicted R parameter, $R_{\rm th}$, to helium content, Y, and coupling constant, $g_{a\gamma}$. This relationship is given by Equation 4.1

$$R_{\rm th}(g_{a\gamma}, Y) = 6.26\, Y - 0.41\, g_{10}^2 - 0.12\,, \tag{4.1}$$

The last formula describes quite well the numerical results. A degeneracy between Y and $g_{a\gamma}$ is observed. R increases linearly as Y , which can be seen in Figure 4.4, and decreases with $g_{a\gamma}^2$.

Table 4.4: Lifetimes and R_{th} calculated from different axion models. In all cases $M/M_{\odot} = 0.82$, $Z = 0.001$, $Y = 0.248$

g_{10}	t_{HB}(Myr)	R
0.00	87.95	1.44
0.30	85.69	1.40
0.50	81.66	1.33
0.75	73.79	1.20
1.00	62.78	1.02

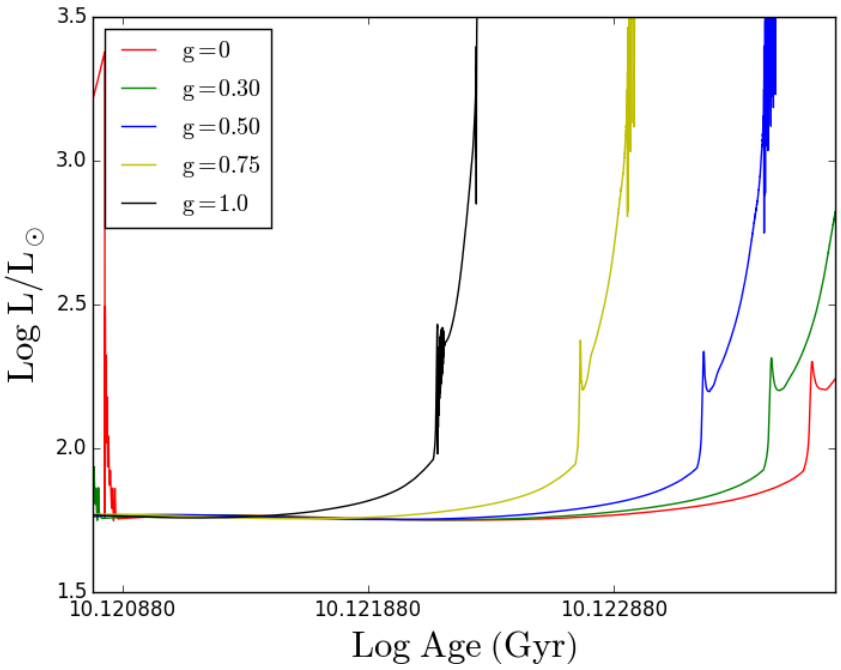

Figure 4.3: Luminosity vs time, during HB, for reference model ($M = 0.82\,M_{\odot}$, $Y = 0.248$, $Z = 0.001$, $g_{10} = 0.00$) and models with the same mass, helium content and metallicity, but different values of g_{10} ($g_{10} = 0.30$, 0.50, 0.75, 1.00).

Table 4.5: Effects of helium initial content, Y, and g_{10} on R_{th}

Y	g_{10}	R_{th}
0.230	0.00	1.32
0.240	0.00	1.38
0.248	0.00	1.44
0.262	0.00	1.52
0.248	0.25	1.41
0.262	0.25	1.49
0.280	0.25	1.61
0.248	1.00	1.02
0.262	1.00	1.11
0.290	1.00	1.28

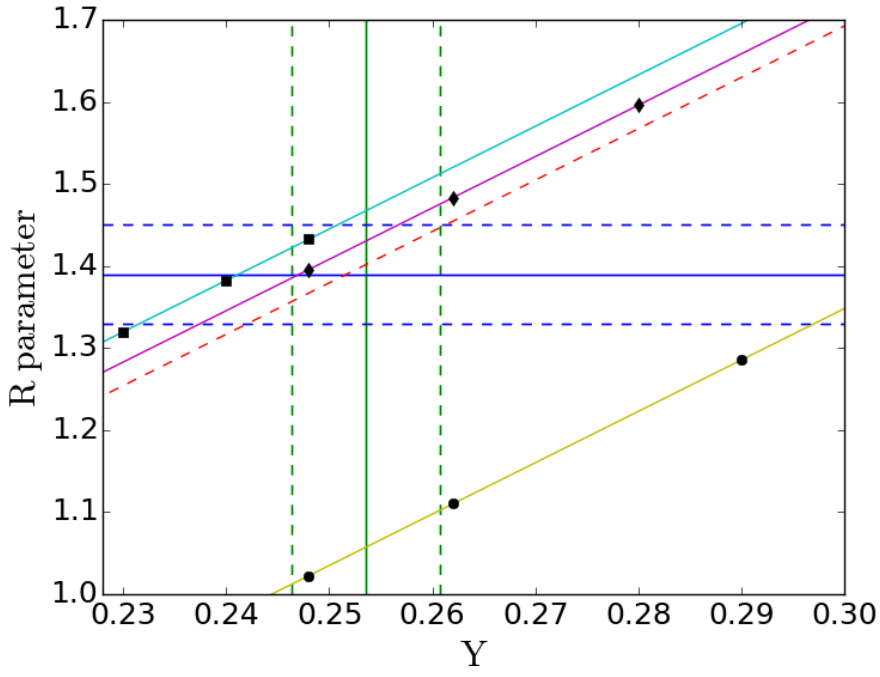

Figure 4.4: Fit of R_{th} to helium mass content. Different models were calculated: $g_{10} = 0.00$, squares; $g_{10} = 0.30$, diamonds; $g_{10} = 1.00$, circles. In all cases a linear behaviour with respect to helium mass fraction is found. The red dashed line corresponds to Equation 4.1 for the case $g_{10} = 0.45$, which is the best possible fit for observational data. Vertical continuous line is central value of Y found by Aver (Aver et al. 2013). Vertical dashed lines are 2σ ranges. Horizontal lines represent the weighted average of R_{obs} parameter obtained from the clusters in Salaris catalog and the 2σ ranges.

4.3 Results for bounds on $g_{a\gamma}$

In order to constrain the axion-photon coupling, we compare the average value of R (R_{obs}) with the theoretical prediction (R_{th}). Assuming that the R_{obs} measurements are distributed as Gaussian variables, one can determine confidence levels for the different quantities. Our results are shown in Figure 4.5.

The vertical lines indicate, respectively, the central Y value determined by Aver et al. (2013) (green solid), and 68% CL (green dotted) and 95 % CL (green dashed curves) uncertainties of Y. The vertical line at $Y = 0.269$ corresponds to the solar value of Y. The other bent curves correspond to the determination of $g_{a\gamma}$ as a function of Y from $R_{\rm th}$ [Equation (4.1)]. In particular, the central red curve has been obtained with $R_{th} = R_{obs}$, while the dotted and the dashed red lines indicate, respectively, the 1σ and the 2σ ranges.

Combining the confidence levels of Y and R_{obs}, we find:

$$g_{a\gamma} = 0.45^{+0.12}_{-0.16} \times 10^{-10}\ \text{GeV}^{-1} \quad (68\%\ \text{CL}) \ . \tag{4.2}$$

Where the value $g_{a\gamma} = 0.45$, corresponds to the best-fit point, and is indicated with a square in Figure 4.5. Moreover, we determine an upper bound:

$$g_{a\gamma} < 0.66 \times 10^{-10}\ \text{GeV}^{-1} \quad (95\%\ \text{CL}) \ . \tag{4.3}$$

Note that in the standard physics scenario, $g_{a\gamma} = 0$, we find $Y = 0.241 \pm 0.005$ which is compatible with the measured Y at 2σ.

Previous bounds from HB lifetime (Raffelt & Dearborn 1987), Cepheids observation (Friedland et al. 2013), and from CAST for light ALPs (Arik et al. 2009; Andriamonje et al. 2007) are also shown in Figure 4.5. Recently, the bound we derive has been reached by the CAST experiment (Anastassopoulos et al. 2017), which obtained a bound of $g_{10} < 0.66$. Moreover, future laboratory research, such as the planned upgrade of the photon regeneration experiment ALPS at DESY (Bähre et al. 2013; Ehret et al. 2010) and the next generation solar axion detector IAXO (Irastorza et al. 2011) will be able, hopefully, to reach the region of the space parameters we have investigated. In Table 4.6 we summarize the various bounds obtained under the different assumptions on Y.

The most important source of systematic error, in the upper bound we have derived, is the adopted helium mass fraction. Certainly the primordial He provides a lower bound to the GCs helium mass fraction. According to our purposes, the bound derived by means of R_{th} is quite an upper limit,

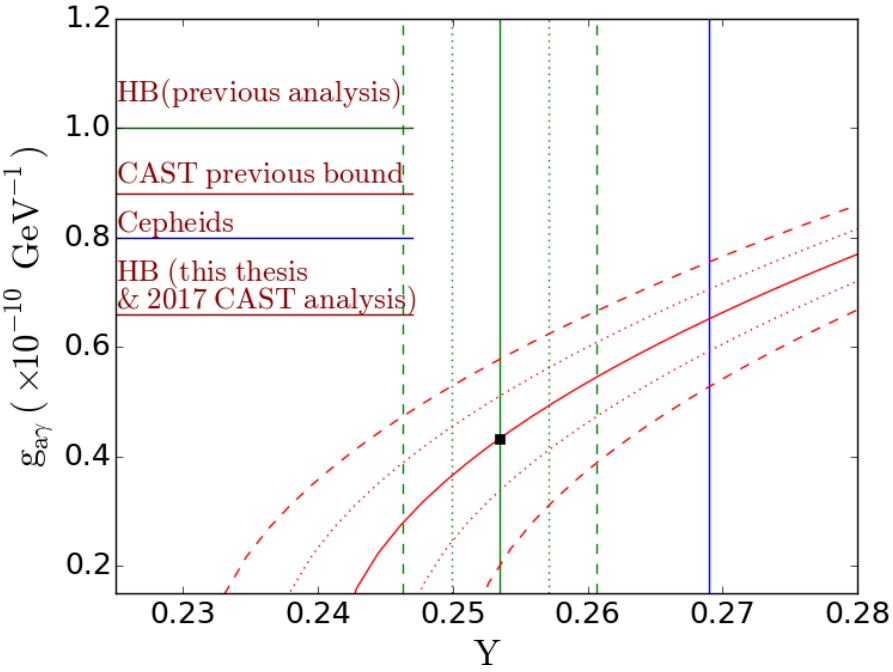

Figure 4.5: R_{th} parameter constraints to Y and $g_{a\gamma}$

taking into account the degeneracy between Y and g_{10} found in the formula 4.1, and the fact the helium mass fraction we use is assumed to be very close to primordial helium content, Y_p. A more stringent constraint can be derived, if an initial helium content relying on Standard Big Bang Nucleosynthesis (SBBN), obtained after Planck results, is taken.

On the other hand, if we assume the He content of the solar system to be the initial helium content of GC stars ($Y_\odot = 0.269$, see, e.g Piersanti et al. (2007)), we find a higher upper bound, namely $g_{a\gamma} < 0.76 \times 10^{-10}$ GeV^{-1} (95% CL). However, the latter limit is an overly conservative assumption which would imply that no chemical evolution occurred during the 8 Gyr elapsed between the GCs and the solar system formation, in contrast to a lot of well-known astronomical evidence.

Thus, it is better to use direct measurements of Y in low metallicity environments which may be considered representative of the chemical composition of the early Galaxy. In this context, optical spectra of low-metallicity H II regions show several He I lines which allow quite an accurate determination of He abundance.

Table 4.6: Bounds of $g_{a\gamma}$ at different confident levels.

		R	Y	g_{10}
bounds from low-Z II regions	up 95%	1.33	0.260	0.66
-	up 68%	1.36	0.257	0.57
-	central value	1.39	0.254	0.45
-	low 68%	1.42	0.251	0.29
-	low 95%	1.45	0.248	0.00
bounds from SBBN	up 95%	1.33	0.2478	0.50
-	up 68%	1.36	0.2475	0.42
-	central value	1.39	0.2472	0.31
-	low 68%	1.42	0.2469	0.15
-	low 95%	1.45	0.2466	0.00
bounds from $Y_\odot$	up 95%	1.33	0.269	0.76
-	up 68%	1.36	0.269	0.71

4.4 Uncertainty analysis

Several sources of uncertainties on the R_{th} parameter must be taken into account to determine their effects on the upper bounds of $g_{a\gamma}$. As stated before, the estimation of R_{th}, requires a detailed knowledge of stellar lifetimes: horizontal branch time, t_{HB}, and upper RGB time, t_{RGB}. These times depend on all the physical processes that produce or dissipate energy in stellar interiors. Specially, these times depend on the rates of the nuclear reactions, mentioned in Chapter 2, $^{14}N\,(p,\gamma)^{15}\,O$, 3α, and $^{12}C\,(\alpha,\gamma)^{16}\,O$, convection, and the existence of a magnetic dipole moment of the neutrino. Due to the fact the bound we derive is an upper one, we are interested in uncertainties which increase R_{th}, and lead to a larger upper bound.

4.4.1 Nuclear reactions

Table 4.7 summarizes the systematic errors due to experimental nuclear reaction rates. The errors on the R parameter induced by these nuclear physics uncertainties are generally small (see last column Table 4.7). It should be noted that possible destructive interference between two destructive sub threshold resonances of the reaction $^{12}C\,(\alpha,\gamma)^{16}\,O$, could imply a reduction in the rate of 50%. However, such a reduction would reduce the need of axion cooling to reconciliate R_{obs} and R_{th}. In this respect, the derived bound for g_{10} remains still valid.

In order to determine a total uncertainty due to the nuclear reactions,

Table 4.7: Effect of nuclear reaction rates on t_{HB}.

Nuclear reaction	Reference	Uncertainty	Uncertainty on R parameter
$^{14}N\,(p,\gamma)^{15}\,O$	Imbriani et al. (2005) Adelberger et al. (2011)	7%	0.5%
3α	Angulo et al. (1999) Fynbo et al. (2005)	10%	1.2%
$^{12}C\,(\alpha,\gamma)$	Kunz et al. (2001) Schürmann et al. (2012)	20%	2.7%

it is necessary to perform a quadratic sum of each uncertainty,

$$\sigma^2_{NR} = \sigma^2_{3\alpha} + \sigma^2_{^{14}N} + \sigma^2_{^{12}C} \tag{4.4}$$

The combined uncertainty of the three nuclear processes gives a value, $\sigma^2_{NR} = 0.002$. This corresponds to an error ± 0.09 at 95% confident level. The effect of the nuclear reaction uncertainty on theoretical R parameter R_{Th} as a function of Y is shown in Figure 4.6.

4.4.2 Convection. Mechanical overshoot

Although we deal with induced overshoot and the formation of a semiconvective layer, by means of the semiconvection algorithm described in Chapter 2, we have to pay attention to mechanical overshoot, because it is the main source of uncertainties of convection models.

In order to quantify mechanical overshoot, we define the overshoot parameter β

$$\beta = -\frac{1}{H_P \cdot \kappa} \quad , \tag{4.5}$$

where κ is the viscosity coefficient and H_P is the so-called "pressure height" (Kippenhahn & Weigert 1990), defined as

$$H_P = -P\frac{dr}{dP} \quad . \tag{4.6}$$

A large mechanical overshoot (which implies $H_p = 1$) can be excluded based on astrophysical evidence. For instance, a large mechanical overshoot implies a too low value of the R_2 parameter, the number ratio of stars in the AGB with respect to stars in the HB phase (Renzini & Fusi Pecci 1988), or there would be in tension with WDs C/O mass fraction ratios, as it is discussed in Straniero et al. (2003). On the contrary, a moderate overshoot ($H_p = 0.25$) would mimic the effect of the semiconvective models we use to

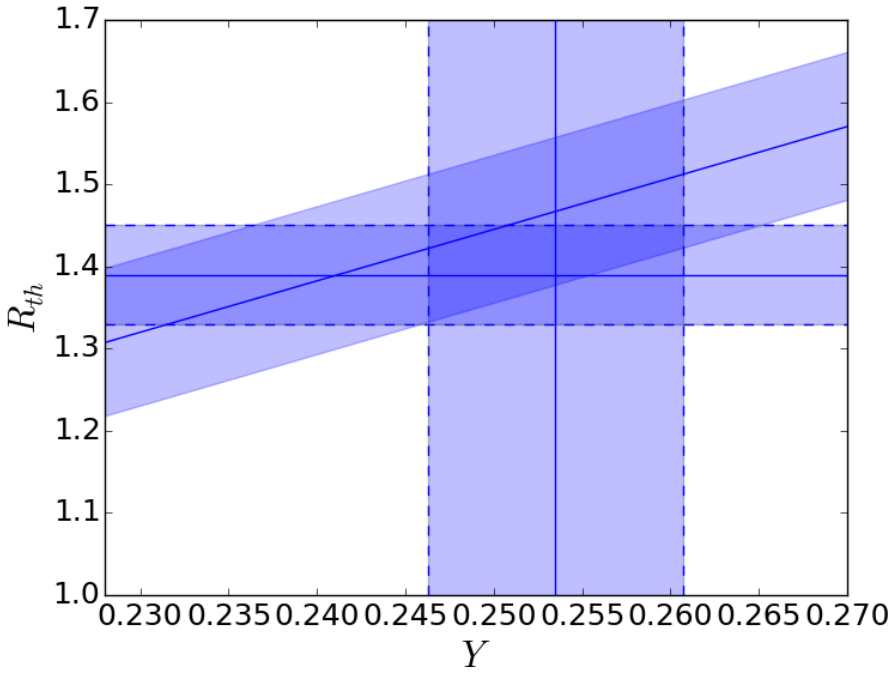

Figure 4.6: Effect of the combined uncertainty of nuclear reactions on the predicted behaviour of R_{th} parameter vs Y for $g_{10} = 0.00$. Vertical lines indicate central Y value (solid) and 2σ limits (dashed lines) determined by Aver et al. (2013). Horizontal lines correspond to R_{obs} (solid) and 2σ ranges(dashed). The lines with the same slope correspond to R_{th} (central) and the upper and lower limits when nuclear reactions uncertainties are considered.

compute the core He burning. Therefore, we conclude it is better not to consider mechanical overshoot uncertainties, on the bases of our treatment of convection.

4.4.3 Neutrino magnetic dipole uncertainty

A hypothetical magnetic dipole moment of neutrino, μ_ν, would imply an enhancement of neutrino losses during low mass stars RGB phase, with the subsequent delay of He-flash, a more massive degenerate He core at the onset of helium ignition and a brighter RGB tip. The constraint $\mu_\nu < 4.5 \times 10^{-12}\,\mu_B$, has been found by Viaux et al. (2013).

The introduction of this "non standard" neutrino rate, should affect the bound, doing it less stringent. A non null value would decrease R_{th}, with respect to the standard situation, reducing the necessity of axions. Therefore, the only reliable approach to obtain an upper bound for $g_{a\gamma}$, is the one keeping $\mu_\nu = 0$, as it has been done in our work.

Chapter 5

Summary and conclusions

In this thesis we accomplished numerical simulations of BSM particles (axions, in particular ALPs) emissions from low mass stars and looked for observable effects of these emissions. We focused on ALPs eventually produced in the core of HB stars through photon coupling (Primakoff process).

Considering theoretical motivations we decided to implement the lagrangian term of axion-photon interaction (which can be considered both: an axion production channel and an energy-sink) in the computation of stellar models with typical mass and composition of the stars currently found in GCs. We performed the computation from the pre-MS till the end of the HB and looked into the axion rates and their effects on the upper RGB and HB evolutionary times, for different values of the axion-photon coupling constant and of the initial helium content of the star. In this way we derived a relationship between the ratio of HB and upper RGB lifetimes (the theoretical R parameter, R_{th}), axion-photon interaction coupling constant ($g_{a\gamma}$), and helium mass fraction (Y).

A degeneracy between Y and $g_{a\gamma}$ was found, because an enhancement of helium content implies R_{th} rises, but on the contrary increasing $g_{a\gamma}$ makes R_{th} smaller. A statistical approach allowed us to deal with the problem of initial helium uncertainties. We used the mean of the observed distribution of the R parameter, R_{obs}, of 39 GCs (Salaris et al. 2004) and the best determination, up to date, of primordial helium mass fraction. This primordial helium mass fraction, Y_p, is stated to be similar to GCs stars initial helium composition, and taking into account this the measurement of Aver et al. (2013) was chosen. Thus, we can invert our formula and calculate axion-photon coupling constant upper bound, using the limits of the observational distributions of R_{obs} and Y_p.

Conclusions

1. We find a relation between the predicted R parameter, R_{th}, initial helium abundance, $g_{a\gamma}$ and Y:

$$R_{\rm th}(g_{a\gamma}, Y) = 6.26\, Y - 0.41\, g_{10}^2 - 0.12 \ . \tag{5.1}$$

2. A degeneracy between $g_{a\gamma}$ and Y is observed. It points to an accurate determination of the initial helium abundance, this being mandatory to derive an accurate value of $g_{a\gamma}$.

3. Comparing R_{th} and the observed R parameter from an updated analysis of 39 GCs, we determine a value for $g_{a\gamma}$:

$$g_{a\gamma} = 0.45^{+0.12}_{-0.16} \times 10^{-10}\ \text{GeV}^{-1} \quad (68\%\ \text{CL}) \ . \tag{5.2}$$

In addition, a new bound has been obtained on the axion-photon coupling constant $g_{a\gamma}$:

$$g_{a\gamma} < 0.66 \times 10^{-10} \text{ GeV}^{-1} \quad (95\% \text{ CL}) \ . \tag{5.3}$$

This bound represents the strongest limit on $g_{a\gamma}$, for axions in a wide mass range. Only in the case of cold dark matter axions is there a stronger constraint, $g_{a\gamma} \lesssim 10^{-15}\ GeV^{-1}$, from Axion Dark Matter Experiment (ADMX), and only for a narrow range around $m_a \sim 1\,\mu$eV. Our bound improves the previous long-standing bound from GCs, $g_{a\gamma} \lesssim 10^{-10}\ GeV^{-1}$, and the more recent one from Cepheid stars, $g_{a\gamma} \lesssim 0.8 \times 10^{-10}\ GeV^{-1}$. This is also the strongest constraint for generic ALPs, except in the extremely low mass region $m_a \lesssim 10^{-10}\ eV$. There, a more stringent limit $g_{a\gamma} \lesssim 10^{-11}\ GeV^{-1}$ or even $g_{a\gamma} \lesssim 3 \times 10^{-12}\ GeV^{-1}$ has been derived from the absence of γ rays from SN 1987A.

4. The combined uncertainties on the theoretical R parameter, R_{th}, of the reactions $^{14}N\,(p,\gamma)^{15}\,O$, 3α, and $^{12}C\,(\alpha,\gamma)^{16}\,O$ is $\sigma = \pm 0.09$ (95% confidence level). In addition, possible destructive interference between two destructive sub threshold resonances of the reaction $^{12}C\,(\alpha,\gamma)^{16}\,O$, could produce a reduction in the rate of 50%. However, this would reduce the need of axion processes to reconciliate R_{obs} and R_{th}. In this respect, the derived bound for $g_{a\gamma}$ remains still valid.
   Due to the fact high mechanical overshoot is excluded by observations and moderate one mimics the effect of the semiconvective algorithm, implemented in our code, we conclude it is better not to consider the effect of mechanical overshoot uncertainties on the bound. Concerning the uncertainties on the bound due to the neutrino magnetic dipole moment, we consider this quantity zero, $\mu_\nu = 0$, in order to derive an upper bound.
   A more detailed study of the uncertainties of the models, systematic and statistical, although in progress, indicates that the central value of $g_{a\gamma}$ is modified, but the upper limit at 2σ is still in agreement with previous value.

Ultralight ALPs with such a small coupling like that reported in this thesis, would play an important role in astrophysics. A particularly hint for these particles has been recently suggested by very- high-energy gamma-ray experiments, even though this problem could also been explained using conventional physics. Indeed, photon-axion conversions in large-scale cosmic magnetic fields would reduce the opacity of the Universe to TeV photons, explaining the anomalous spectral hardening found in the very-high- energy gamma-ray spectra. In particular, for realistic models of the cosmic

magnetic field, this scenario would require $g_{a\gamma} \gtrsim 0.2 \times 10^{-10}\ GeV^{-1}$ and $m_a \lesssim 10^{-7}$ eV.

Remarkably, the coupling ranges discussed in this thesis are accessible to new independent laboratory research, such as the planned upgrade of the ALPS experiment at DESY, and the next generation solar axion detector IAXO. Recently a new bound has been found by CAST collaboration (Anastassopoulos et al. 2017), which now reaches similar levels with respect to the bound reported in this thesis.

Bibliography

Adelberger, E. G., García, A., Robertson, R. G. H., et al. 2011, Reviews of Modern Physics, 83, 195

Alexander, D. R. & Ferguson, J. W. 1994, ApJ, 437, 879

Anastassopoulos, V. et al. 2017, Nature Phys.

Andriamonje, S., Aune, S., Autiero, D., et al. 2007, Journal of Cosmology and Astroparticle Physics, 2007, 010

Angulo, C., Arnould, M., Rayet, M., et al. 1999, Nuclear Physics A, 656, 3

Archidiacono, M., Hannestad, S., Mirizzi, A., Raffelt, G., & Wong, Y. Y. Y. 2013, J. Cosmology Astropart. Phys., 10, 20

Arik, E., Aune, S., Autiero, D., et al. 2009, Journal of Cosmology and Astroparticle Physics, 2009, 008

Aver, E., Olive, K. A., Porter, R., & Skillman, E. D. 2013, Journal of Cosmology and Astroparticle Physics, 2013, 017

Babul, A. & Lee, M. H. 1991, MNRAS, 250, 407

Baker, K., Cantatore, G., Cetin, S. A., et al. 2013, Annalen der Physik, 525, A93

Bernabei, R., Belli, P., Cappella, F., et al. 2008, European Physical Journal C, 56, 333

Bertone, G. & Silk, J. 2010, Particle dark matter, ed. G. Bertone (Cambridge University Press), 3

Böhm-Vitense, E. 1958, ZAp, 46, 108

Buonanno, R., Buzzoni, A., Corsi, C. E., Fusi Pecci, F., & Sandage, A. R. 1986, Mem. Soc. Astron. Italiana, 57, 391

Buzzoni, A., Pecci, F. F., Buonanno, R., & Corsi, C. E. 1983, A&A, 128, 94

Bähre, R., Döbrich, B., Dreyling-Eschweiler, J., et al. 2013, Journal of Instrumentation, 8, T09001

Carosi, G., Friedland, A., Giannotti, M., et al. 2013, ArXiv e-prints

Castelli, F. & Kurucz, R. L. 2004, ArXiv Astrophysics e-prints

Caughlan, G. R. & Fowler, W. A. 1988, Atomic Data and Nuclear Data Tables, 40, 283

Cheng, H.-Y. 1988, Phys. Rep., 158, 1

Clayton, D. D. 1983, Principles of stellar evolution and nucleosynthesis (University of Chicago Press, 1983)

Costantini, H., Deboer, R. J., Azuma, R. E., et al. 2010, Phys. Rev. C, 82, 035802

Cox, J. P. & Giuli, R. T. 1968, Principles of stellar structure (New York: Gordon and Breach)

Cristallo, S., Piersanti, L., Straniero, O., et al. 2011, ApJS, 197, 17

Cristallo, S., Straniero, O., Gallino, R., et al. 2009, ApJ, 696, 797

de Angelis, A., Roncadelli, M., & Mansutti, O. 2007, Phys. Rev. D, 76, 121301

Dewitt, H. E., Graboske, H. C., & Cooper, M. S. 1973, ApJ, 181, 439

Di Valentino, E., Giusarma, E., Lattanzi, M., Melchiorri, A., & Mena, O. 2014, Phys. Rev. D, 90, 043534

Dine, M., Fischler, W., & Srednicki, M. 1981, Physics Letters B, 104, 199

Drees, M. & Gerbier, G. 2012, ArXiv e-prints

Duffy, L. D., Sikivie, P., Tanner, D. B., et al. 2006, Phys. Rev. D, 74, 012006

Ehret, K., Frede, M., Ghazaryan, S., et al. 2010, Physics Letters B, 689, 149

Esposito, S., Mangano, G., Miele, G., Picardi, I., & Pisanti, O. 2003, Nuclear Physics B, 658, 217

Essey, W., Kalashev, O. E., Kusenko, A., & Beacom, J. F. 2010, Phys. Rev. Lett., 104, 141102

Essey, W. & Kusenko, A. 2010, Astroparticle Physics, 33, 81

Essig, R., Jaros, J. A., Wester, W., et al. 2013, ArXiv e-prints

Friedland, A., Giannotti, M., & Wise, M. 2013, Phys. Rev. Lett., 110, 061101

Fukugita, M., Watamura, S., & Yoshimura, M. 1982, Phys. Rev. Lett., 48, 1522

Fynbo, H. O. U., Diget, C. A., Bergmann, U. C., et al. 2005, Nature, 433, 136

Gamow, G. & Schoenberg, M. 1941, Physical Review, 59, 539

Giannotti, M., Irastorza, I., Redondo, J., & Ringwald, A. 2016, J. Cosmology Astropart. Phys., 5, 057

Görres, J., Arlandini, C., Giesen, U., et al. 2000, Phys. Rev. C, 62, 055801

Graboske, H. C., Dewitt, H. E., Grossman, A. S., & Cooper, M. S. 1973, ApJ, 181, 457

Graham, P. W., Irastorza, I. G., Lamoreaux, S. K., Lindner, A., & van Bibber, K. A. 2015, Annual Review of Nuclear and Particle Science, 65, 485

Gratton, R. G., Carretta, E., & Bragaglia, A. 2012, A&A Rev., 20, 50

Hayashi, E. & White, S. D. M. 2006, MNRAS, 370, L38

Henyey, L., Vardya, M. S., & Bodenheimer, P. 1965, ApJ, 142, 841

Horns, D. & Meyer, M. 2012, Journal of Cosmology and Astroparticle Physics, 2012, 033

Iben, I. 1968, Nature, 220, 143

Iben, I. & Rood, R. T. 1969, Nature, 223, 933

Iben, Jr., I. 2013, Stellar Evolution Physics, Volume 1: Physical Processes in Stellar Interiors (University of Chicago Press.)

Iglesias, C. A. & Rogers, F. J. 1996, ApJ, 464, 943

Imbriani, G., Costantini, H., Formicola, A., et al. 2005, European Physical Journal A, 25, 455

Irastorza, I., Avignone, F., Caspi, S., et al. 2011, Journal of Cosmology and Astroparticle Physics, 2011, 013

Isern, J., García-Berro, E., Torres, S., & Catalán, S. 2008, ApJ, 682, L109

Itoh, N., Totsuji, H., & Ichimaru, S. 1977, ApJ, 218, 477

Itoh, N., Totsuji, H., Ichimaru, S., & Dewitt, H. E. 1979, ApJ, 234, 1079

Izotov, Y. I., Stasińska, G., & Guseva, N. G. 2013, A&A, 558, A57

Jaeckel, J. & Ringwald, A. 2010, Annual Review of Nuclear and Particle Science, 60, 405

Jungman, G., Kamionkowski, M., & Griest, K. 1996, Phys. Rep., 267, 195

Kaeppeler, F., Wiescher, M., Giesen, U., et al. 1994, ApJ, 437, 396

Kawasaki, M. & Nakayama, K. 2013, Annual Review of Nuclear and Particle Science, 63, 69

Kim, J. E. 1979, Physical Review Letters, 43, 103

Kim, J. E. 1987, Phys. Rep., 150, 1

Kippenhahn, R. & Weigert, A. 1990, Stellar Structure and Evolution (Berlin-Heidelberg-New York: Springer-Verlag), 192

Kowalska, K., Roszkowski, L., Sessolo, E. M., Trojanowski, S., & Williams, A. J. 2015, ArXiv e-prints

Kunz, R., Jaeger, M., Mayer, A., et al. 2001, Physical Review Letters, 86, 3244

Kuster, M., Raffelt, G., & Beltrán, B., eds. 2008, Lecture Notes in Physics, Berlin Springer Verlag, Vol. 741, Axions

Langanke, K., Thielemann, F.-K., Wiescher, M., et al. 2006, Nuclear Physics A, 777, 311

Ledoux, P. 1947, AJ, 52, 155

Lodders, K. 2003, ApJ, 591, 1220

Lopes, I., Casanellas, J., & Eugénio, D. 2011, Phys. Rev. D, 83, 063521

Massó, E., Rota, F., & Zsembinszki, G. 2002, Phys. Rev. D, 66, 023004

Olive, K. A. & Steigman, G. 1995, ApJS, 97, 49

Peccei, R. D. & Quinn, H. R. 1977a, Phys. Rev. D, 16, 1791

Peccei, R. D. & Quinn, H. R. 1977b, Physical Review Letters, 38, 1440

Perlmutter, S., Aldering, G., della Valle, M., et al. 1998, Nature, 391, 51

Persic, M., Salucci, P., & Stel, F. 1996a, MNRAS, 283, 1102

Persic, M., Salucci, P., & Stel, F. 1996b, MNRAS, 281, 27

Piersanti, L., Straniero, O., & Cristallo, S. 2007, A&A, 462, 1051

Planck Collaboration, Ade, P. A. R., Aghanim, N., et al. 2014, A&A, 571, A1

Potekhin, A. Y., Baiko, D. A., Haensel, P., & Yakovlev, D. G. 1999, A&A, 346, 345

Raffelt, G. G. 1986, Phys. Rev. D, 33, 897

Raffelt, G. G. 1990, Phys. Rep., 198, 1

Raffelt, G. G. 1996, Stars as laboratories for fundamental physics : the astrophysics of neutrinos, axions, and other weakly interacting particles (University of Chicago Press.)

Raffelt, G. G. & Dearborn, D. S. P. 1987, Phys. Rev. D, 36, 2211

Renzini, A. & Fusi Pecci, F. 1988, ARA&A, 26, 199

Rubin, V. C., Ford, W. K. J., & . Thonnard, N. 1980, ApJ, 238, 471

Salaris, M., Riello, M., Cassisi, S., & Piotto, G. 2004, A&A, 420, 911

Schürmann, D., Gialanella, L., Kunz, R., & Strieder, F. 2012, Physics Letters B, 711, 35

Shifman, M. A., Vainshtein, A. I., & Zakharov, V. I. 1980, Nuclear Physics B, 166, 493

Sikivie, P. 1983, Physical Review Letters, 51, 1415

Sikivie, P. 2008, in Lecture Notes in Physics, Berlin Springer Verlag, Vol. 741, Axions, ed. M. Kuster, G. Raffelt, & B. Beltrán, 19

Sikivie, P. & Yang, Q. 2009, Physical Review Letters, 103, 111301

Sparks, W. M. & Endal, A. S. 1980, ApJ, 237, 130

Springel, V., Frenk, C. S., & White, S. D. M. 2006, Nature, 440, 1137

Straniero, O. 1988, A&AS, 76, 157

Straniero, O., Domínguez, I., Imbriani, G., & Piersanti, L. 2003, ApJ, 583, 878

Straniero, O., Gallino, R., & Cristallo, S. 2006, Nuclear Physics A, 777, 311

Turner, M. S. 1987, Phys. Rev. Lett., 59, 2489

Viaux, N., Catelan, M., Stetson, P. B., et al. 2013, Phys. Rev. Lett., 111, 231301

Weinberg, S. 1978, Phys. Rev. Lett., 40, 223

Zwicky, F. 1933, Helvetica Physica Acta, 6, 110

Acronyms

ADMX Axion Dark Matter Experiment . . . 77
AGB Asymptotic Giant Branch . . . 62
ALP Axion-Like Particle . . . 7
ALPS Any Light Particle Search . . . 10
ALPS-II Any Light Particle Search II . . . 4
BSM Beyond Standard Model . . . 3
CAST CERN Axion Solar Telescope . . . 9
CMD Colour-Magnitude Diagram . . . 40
CP Charge Parity . . . 2
DFSZ Dine, Fischler, Srednick and Zhitnitskii . . . 8
DM Dark Matter . . . 2
EOS Equation of State . . . 16
GC Globular Cluster . . . 12
HB Horizontal Branch . . . 31
IAXO International Axion Observatory . . . 4
KSVZ Kim, Shiftman, Vainshtein and Zakharov . . . 8
LHC Large Hadron Collider . . . 3
LSW Light Shining through the Walls . . . 10
MS Main Sequence . . . 40
pre-MS pre-Main Sequence . . . 40
QCD Quantum Chromodynamics . . . 4
RGB Red Giant Branch . . . 40
SBBN Standard Big Bang Nucleosynthesis . . . 70
SM Standard Model . . . 2
WD White Dwarf . . . 3
WIMP Weakly Interacting Massive Particle . . . 3
WISP Weakly Interacting Slim Particle . . . 3
ZAHB Zero Age Horizontal Branch . . . 49